

---

# High dimensional analysis reveals conservative sharpening and a stochastic edge of stability

---

**Atish Agarwala**  
Google DeepMind  
thetish@google.com

**Jeffrey Pennington**  
Google DeepMind  
jpennin@google.com

## Abstract

Recent empirical and theoretical work has shown that the dynamics of the large eigenvalues of the training loss Hessian have some remarkably robust features across models and datasets in the full batch regime. There is often an early period of *progressive sharpening* where the large eigenvalues increase, followed by stabilization at a predictable value known as the *edge of stability*. Previous work showed that in the stochastic setting, the eigenvalues increase more slowly - a phenomenon we call *conservative sharpening*. We provide a theoretical analysis of a simple high-dimensional model which shows the origin of this slowdown. We also show that there is an alternative *stochastic edge of stability* which arises at small batch size that is sensitive to the trace of the Neural Tangent Kernel rather than the large Hessian eigenvalues. We conduct an experimental study which highlights the qualitative differences from the full batch phenomenology, and suggests that controlling the stochastic edge of stability can help optimization.

## 1 Introduction

Despite rapid advances in the capabilities of machine learning systems, a large open question about training remains: what makes stochastic gradient descent work in deep learning? Much recent work has focused on understanding learning dynamics through the lens of the loss landscape geometry. The Hessian of the training loss with respect to the parameters changes significantly over training, and its statistics are intimately linked to optimization choices (Ghorbani et al., 2019; Gilmer et al., 2022).

In the full batch setting, there are two robust observations about eigenvalues of the loss Hessian: *progressive sharpening* and stabilization at the *edge of stability* (EOS) (Cohen et al., 2022a,b). Progressive sharpening refers to the tendency of Hessian eigenvalues to increase at early times. After this period of increase, the maximum eigenvalue  $\lambda_{max}$  tends to stabilize around  $2/\eta$  - the maximum value possible that still admits convergent dynamics in the convex setting. The EOS stabilization phenomenology can be explained theoretically through the negative feedback between  $\lambda_{max}$  and the parameter changes in the largest eigendirection of the Hessian (Damian et al., 2022; Agarwala et al., 2022).

The phenomenology is more complicated in the minibatch setting (SGD). For one, progressive sharpening decreases in strength as batch size decreases - a phenomenon which we dub *conservative sharpening* (Jastrzebski et al., 2018; Cohen et al., 2022a). In addition, there is theoretical and experimental evidence that the stochastic nature of the gradients suggests that quantities other than  $\lambda_{max}$ , such as the *trace* of the Hessian, are important for long-time convergence and stability (Jastrzebski et al., 2020; Wu et al., 2022). This observation has led to attempts to define a *stochastic edge of stability* (S-EOS) which can provide insight into loss landscape geometry in the SGD setting (Wu & Su, 2023; Mulayoff & Michaeli, 2023).

In parallel, there has been progress in understanding aspects of SGD in simple but high-dimensional models. The theory of infinitely-wide neural networks has shown that in the appropriate limit, model training resembles gradient-based training of kernel methods (Jacot et al., 2018; Lee et al., 2019; Adlam & Pennington, 2020). More recent work has studied the dynamics of SGD in convex models where the number of datapoints and the number of parameters scale to infinity at the same rate (Mei et al., 2019; Paquette et al., 2021, 2022a,b; Ben Arous et al., 2022; Arnaboldi et al., 2023). These theoretical works have found tight stability/convergence conditions in this high-dimensional regime – a regime that is increasingly important in the current landscape of increasing model and dataset sizes.

In this work, we provide evidence that an S-EOS stabilization phenomenon is useful for understanding neural network training dynamics. We use theoretical analysis to show the following:

- There is a *stochastic edge of stability* (S-EOS) which in the MSE setting is controlled by a scalar  $\mathcal{K}$  which we call the *noise kernel norm*.
- Conservative sharpening depends on the statistics of both the Jacobian and its gradient, and provides stronger suppression on larger eigenvalues.

These theoretical findings suggest there is a practical regime where S-EOS effects are important in training models. We then demonstrate the following experimentally:

- $\mathcal{K}$  self-stabilizes near the critical value 1, giving us an S-EOS stabilization which is qualitatively distinct from stabilization of  $\lambda_{max}$  in the original EOS.
- For small batch size the behavior of  $\mathcal{K}$  is a slowly varying function of  $\eta/B$ .
- $\mathcal{K}$  is predictive of training outcomes across a variety of model sizes, and with additional effects like momentum and learning rate schedules.

We conclude with a discussion of how quantities like  $\mathcal{K}$  might be useful in understanding curvature dynamics of SGD in more general scenarios.

## 2 SGD in the quadratic regression model

In this section we establish the basic theoretical model we use for the analyses in Sections 3 and 4. We follow the approach of (Agarwala & Dauphin, 2023) and study phenomenology using a *quadratic regression model* - a minimal non-linear model which still shows key non-linear phenomenology (Zhu et al., 2022; Agarwala et al., 2022).

### 2.1 Quadratic regression model

Given a  $P$ -dimensional parameter vector  $\theta$  and a  $D$ -dimensional output function  $\mathbf{f}(\theta)$ , we can write  $\mathbf{f}$  as a Taylor expansion around  $\theta_0$ . Taking the first two terms of the expansion only, we have the *quadratic regression model*:

$$\mathbf{f}(\theta) = \mathbf{f}(\theta_0) + \mathbf{J}_0[\theta - \theta_0] + \frac{1}{2}\mathbf{Q}[\theta - \theta_0, \theta - \theta_0]. \quad (1)$$

Here  $\mathbf{J}_0 \equiv \frac{\partial \mathbf{f}}{\partial \theta}(\theta_0)$  is the  $D \times P$ -dimensional Jacobian at  $\theta_0$ , and  $\mathbf{Q} \equiv \frac{\partial^2 \mathbf{f}}{\partial \theta \partial \theta'}(\theta_0)$  is the  $D \times P \times P$ -dimensional *model curvature*. For  $\mathbf{Q} = 0$ , we recover a linear regression model. For convenience we assume, WLOG, that  $\theta_0 = 0$ .

We will generally interpret the  $D$  outputs as coming from  $D$  inputs with 1-dimensional outputs; however, our analysis naturally covers the case of  $C$ -dimensional outputs on  $D/C$  datapoints.

### 2.2 SGD dynamics

We focus on the case of MSE loss. Given training targets  $\mathbf{y}_{tr}$ , the full loss is given by

$$\mathcal{L}(\theta) = \frac{1}{2D} \|\mathbf{z}\|^2, \quad \mathbf{z} \equiv \mathbf{f}(\theta) - \mathbf{y}_{tr}. \quad (2)$$

We will consider training with minibatch SGD with batch size  $B$ , which can be described as follows. Let  $\mathbf{P}_t$  be a sequence of random, i.i.d. diagonal matrices with exactly  $B$  random 1s on the diagonal,

and 0s everywhere else. Then the loss for minibatch  $t$  is given by

$$\mathcal{L}_{mb,t}(\boldsymbol{\theta}) = \frac{1}{2B} \mathbf{z}^\top \mathbf{P}_t \mathbf{z}. \quad (3)$$

The update rule for minibatch gradient descent is

$$\boldsymbol{\theta}_{t+1} - \boldsymbol{\theta}_t = -\frac{\eta}{B} \mathbf{J}_t^\top \mathbf{P}_t \mathbf{z}_t. \quad (4)$$

where  $\mathbf{J} = \partial \mathbf{z} / \partial \boldsymbol{\theta}$ , the Jacobian at the current  $\boldsymbol{\theta}$ . Under this update rule, the dynamics can be expressed exactly in terms of  $\mathbf{z}_t$  and  $\mathbf{J}_t$  alone:

$$\begin{aligned} \mathbf{z}_{t+1} - \mathbf{z}_t &= -\frac{\eta}{B} \mathbf{J}_t \mathbf{J}_t^\top \mathbf{P}_t \mathbf{z}_t + \frac{\eta^2}{2B^2} \mathbf{Q}(\mathbf{J}_t^\top \mathbf{P}_t \mathbf{z}_t, \mathbf{J}_t^\top \mathbf{P}_t \mathbf{z}_t) \\ \mathbf{J}_{t+1} - \mathbf{J}_t &= -\frac{\eta}{B} \mathbf{Q}(\mathbf{J}_t^\top \mathbf{P}_t \mathbf{z}_t, \cdot). \end{aligned} \quad (5)$$

This lets us understand the joint dynamics of the loss and geometry directly, which will aid conceptual understanding.

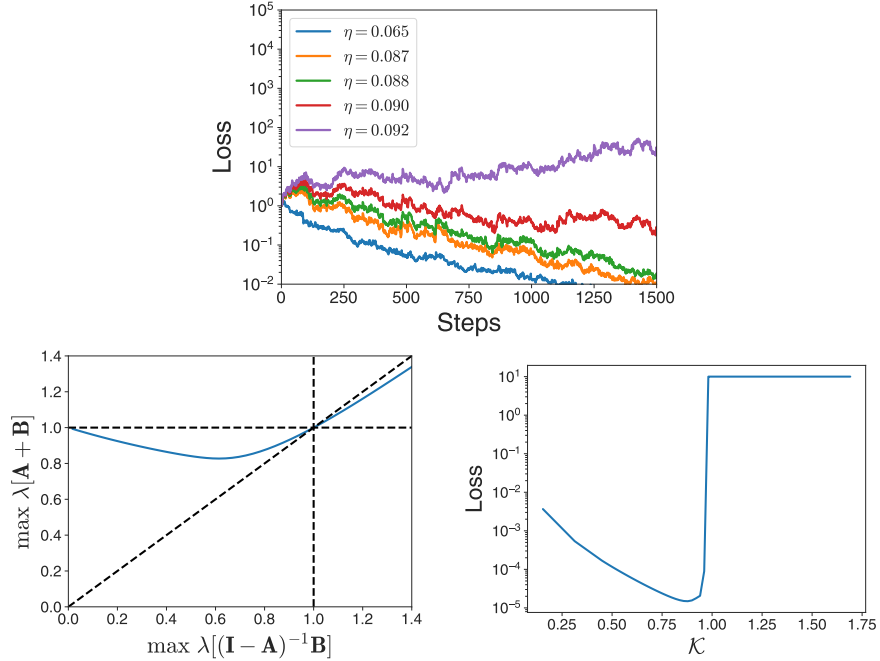


Figure 1: SGD trajectories for linear regression show divergence due to stochastic effects as  $\eta$  is increased (top,  $B = 5$ ,  $D = 100$ ,  $P = 120$ , i.i.d. Gaussian  $\mathbf{J}$ ).  $\mathcal{K}$  interpolates from 0 at small learning rate, to value 1 precisely when  $\lambda_{max}[\mathbf{A} + \mathbf{B}] = 1$  (bottom left). Loss after  $10^4$  steps diverges for  $\mathcal{K} > 1$  (bottom right, plot saturated  $10^1$  for convenience).

### 3 The stochastic edge of stability

In the deterministic setting, the edge of stability (EOS) is derived by performing stability analysis of the loss under full batch (GD) dynamics about a minimum on a convex model. In this section, we derive a stability condition for SGD in an analogous fashion. In the stochastic setting, we will focus on the long-time behavior of the *moments* of the network outputs - where the averages are taken over the sampling of the minibatches.

We will define a *noise kernel norm*  $\mathcal{K}$  which characterizes the stability of *second moments* of the residuals  $\mathbf{z}_t$  under SGD noise. The resulting measure will range from 0 in the full batch SGD case to 1 at the stability threshold - analogous to the role the normalized eigenvalue  $\eta \lambda_{max} / 2$  plays in the full batch case.

### 3.1 First moment stability defines deterministic EOS

More concretely, consider the model from Section 2 with  $\mathbf{Q} = 0$ . This is a linear regression model. From Equation 5,  $\mathbf{J}$  is fixed and our dynamical equation is:

$$\mathbf{z}_{t+1} - \mathbf{z}_t = -\frac{\eta}{B} \mathbf{J} \mathbf{J}^\top \mathbf{P}_t \mathbf{z}_t. \quad (6)$$

We can understand the behavior of this system by averaging  $\mathbf{z}$  with respect to the  $\mathbf{P}$ . The first moment evolves as:

$$\mathbb{E}_{\mathbf{P}}[\mathbf{z}_{t+1} - \mathbf{z}_t | \mathbf{z}_t, \mathbf{J}_t] = -\eta \hat{\Theta} \mathbb{E}_{\mathbf{P}}[\mathbf{z}_t] \quad (7)$$

where we define the (empirical) *neural tangent kernel* (NTK) as  $\hat{\Theta} \equiv \frac{1}{D} \mathbf{J} \mathbf{J}^\top$  (Jacot et al., 2018).

This gives us a linear recurrence equation for  $\mathbb{E}[\mathbf{z}_t]$ , which converges to 0 if and only if  $\eta \lambda_{max} < 2$  for the largest eigenvalue  $\lambda_{max}$  of  $\hat{\Theta}$ . This is exactly the full-batch (deterministic) EOS condition. Therefore we can interpret the ‘‘standard’’ EOS as a stability condition on the first moment of  $\mathbf{z}$ .

### 3.2 Second moment stability defines stochastic EOS

We now describe a method to find *noise-driven* instabilities in the dynamics of Equation 6 which have no full-batch analogue. These instabilities are found by analyzing the long-time behavior of the *second moments* of  $\mathbf{z}$ . We will find a stability condition in terms of  $\hat{\Theta}$ ,  $\eta$ , and  $B$  which we will call the *stochastic EOS* (S-EOS).

The approach of studying stability of the second moment was studied previously in (Ma & Ying, 2021; Mulayoff & Michaeli, 2023); these focused on local, weight space analysis. Instead, we will perform a global, function space analysis most similar to Paquette et al. (2021) - which focused on a specific, high-dimensional, rotationally invariant limit. Our analysis makes no such assumptions.

The covariance of the residuals evolves as:

$$\begin{aligned} \mathbb{E}_{\mathbf{P}}[\mathbf{z}_{t+1} \mathbf{z}_{t+1}^\top | \mathbf{z}_t] &= \mathbf{z}_t \mathbf{z}_t^\top - \eta \left( \hat{\Theta} \mathbf{z}_t \mathbf{z}_t^\top + \mathbf{z}_t \mathbf{z}_t^\top \hat{\Theta} \right) \\ &+ \tilde{\beta} \beta^{-1} \eta^2 \hat{\Theta} \mathbf{z}_t \mathbf{z}_t^\top \hat{\Theta} + (\beta^{-1} - \tilde{\beta} \beta^{-1}) \eta^2 \hat{\Theta} \text{diag}[\mathbf{z}_t \mathbf{z}_t^\top] \hat{\Theta} \end{aligned} \quad (8)$$

where  $\beta \equiv B/D$  is the batch fraction, and  $\tilde{\beta} \equiv (B-1)/(D-1)$ . Inspecting Equation 8, we see that the covariance evolves as a linear dynamical system, whose corresponding linear operator we denote will denote as  $\mathbf{T}$ .

The stability of the dynamics is controlled by  $\max \|\lambda[\mathbf{T}]\|$ , the largest eigenvalue (by magnitude) of  $\mathbf{T}$ . If  $\max \|\lambda[\mathbf{T}]\| < 1$ , the dynamics are stable ( $\lim_{t \rightarrow \infty} \mathbb{E}_{\mathbf{P}}[\mathbf{z}_t \mathbf{z}_t^\top] = 0$ ). If  $\max \|\lambda[\mathbf{T}]\| > 1$ , then the dynamics diverge ( $\lim_{t \rightarrow \infty} \mathbb{E}_{\mathbf{P}}[\mathbf{z}_t \mathbf{z}_t^\top] = \infty$ ). Note that the trace of the covariance is the expected loss.

We say a system is at the *stochastic edge of stability* (S-EOS) if both  $\eta \max \lambda[\hat{\Theta}] < 2$  and  $\max \|\lambda[\mathbf{T}]\| = 1$ . In the full batch setting ( $\beta = 1$ ),  $\max \|\lambda[\mathbf{T}]\| = 1$  if and only if  $\eta \max \lambda[\hat{\Theta}] = 2$ , so the two conditions are equivalent. However if  $\beta < 1$ , then the last term in Equation 8 contributes to  $\max \|\lambda[\mathbf{T}]\|$ , and there are systems which are unstable due to the effects of SGD noise alone (Figure 1, left).

### 3.3 Noise kernel norm decomposition

In general,  $\mathbf{T}$  is a  $D^2 \times D^2$  matrix, whose entries are derived from  $P$ -dimensional inner products. This can quickly become intractable for large  $D$  and  $P$ . Additionally,  $\max \|\lambda[\mathbf{T}]\|$  does *not* distinguish between noise-driven and deterministically-driven instabilities. We will use a  $D \times D$  dimensional approximation to the dynamics to define the *noise kernel norm*  $\mathcal{K}$  - an interpretable measure of the influence of noise in the optimization dynamics and a good predictor of the S-EOS.

Consider the rotated covariance  $\mathbf{S}_t \equiv \mathbf{V}^\top \mathbb{E}_{\mathbf{P}}[\mathbf{z}_t \mathbf{z}_t^\top] \mathbf{V}$ , where  $\mathbf{V}$  comes from the eigendecomposition  $\hat{\Theta} = \mathbf{V} \mathbf{A} \mathbf{V}^\top$ . We define the normalized diagonal  $\tilde{\mathbf{p}} \equiv \mathbf{A}^+ \text{diag}(\mathbf{S})$ , where  $\text{diag}(\mathbf{S})$  is the vector obtained from the diagonal of  $\mathbf{S}$ . Consider the dynamics of  $\tilde{\mathbf{p}}$  under the linear operator  $\mathbf{T}$ , restricted to  $\tilde{\mathbf{p}}$ . That is, we ignore any contributions to the dynamics from terms like  $\mathbb{E}_{\mathbf{P}}[(\mathbf{v} \cdot \mathbf{z}_t)(\mathbf{v}' \cdot \mathbf{z}_t)]$  for

distinct eigenvectors  $\mathbf{v}$  and  $\mathbf{v}'$  of  $\hat{\Theta}$ . We have (Appendix A.2):

$$\begin{aligned}\tilde{\mathbf{p}}_{t+1} &= (\mathbf{A} + \mathbf{B})^t \tilde{\mathbf{p}}_0, \quad \mathbf{A} \equiv (\mathbf{I} - \eta\mathbf{\Lambda})^2 + (\tilde{\beta}\beta^{-1} - 1)\mathbf{\Lambda}^2 \\ \mathbf{B} &\equiv (\beta^{-1} - \tilde{\beta}\beta^{-1})\eta^2\mathbf{\Lambda}\mathbf{C}\mathbf{\Lambda}.\end{aligned}\tag{9}$$

Here  $\mathbf{A}$  (the deterministic contribution) and  $\mathbf{B}$  (the stochastic contribution) are both PSD matrices, and  $\mathbf{C}_{\beta\mu} \equiv \sum_{\alpha} \mathbf{V}_{\alpha\beta}^2 \mathbf{V}_{\alpha\mu}^2$  gives the noise-induced coupling between the eigenmodes of  $\hat{\Theta}$ . The largest eigenvalue of this linear system gives us an approximation of  $\max \|\lambda[\mathbf{T}]\|$ .

Instead of computing  $\max \lambda[\mathbf{A} + \mathbf{B}]$  directly, we define the *noise kernel norm*  $\mathcal{K}$ , which interpolates from 0 for  $\beta = 1$  (no noise) to  $\mathcal{K} = 1$  at the S-EOS. In Appendix A.3 we prove the following theorem:

**Theorem 3.1.** *If the diagonal of  $\mathbf{S}$  is governed by Equation 9, then  $\lim_{t \rightarrow \infty} \mathbb{E}_{\mathbf{P}}[\mathbf{z}_t \mathbf{z}_t^{\top}] = 0$  for any initialization  $\mathbf{z}_t$  if and only if  $\|\mathbf{A}\|_{op} < 1$  and  $\mathcal{K} < 1$  where*

$$\mathcal{K} \equiv \max \lambda [(\mathbf{I} - \mathbf{A})^{-1} \mathbf{B}]\tag{10}$$

for the PSD matrices  $\mathbf{A}$  and  $\mathbf{B}$  defined above.  $\mathcal{K}$  is always non-negative.

$\mathcal{K}$  is a measure of the SGD-induced noise in the dynamics, normalized by the S-EOS. This is analogous to the normalized eigenvalue  $\eta\lambda_{max}$  used in analysis of the deterministic EOS (Agarwala et al., 2022; Damian et al., 2022). When the noise is small (large  $B$  or small  $\eta$ ),  $\mathcal{K}$  is also small. This is more informative than  $\max \lambda[\mathbf{A} + \mathbf{B}]$ , which is often close to 1 even in the deterministic setting (Figure 1, middle), where it is given by  $(1 - \eta\lambda_{min})^2$  for the minimum eigenvalue  $\lambda_{min}$  of  $\hat{\Theta}$ . Even though  $\mathcal{K}$  is derived from an approximation of  $\mathbf{T}$ , the S-EOS is often well-predicted by  $\mathcal{K} = 1$  even for small systems (Figure 1, right,  $D = 100$ ).

As we will show later, these properties of  $\mathcal{K}$  make it suitable for analysis of the effects of SGD in non-convex settings.

### 3.4 Approximations of $\mathcal{K}$

A key difference between the S-EOS and the deterministic EOS is that the S-EOS depends on the whole spectrum of  $\hat{\Theta}$ . We can show this directly by computing approximations to  $\mathcal{K}$ . These will have the additional benefit of being easy to compute, especially on real neural network setups.

In the high-dimensional limit, Paquette et al. (2021) showed that  $\tilde{\beta} \approx \beta$  and  $\mathbf{C} \approx \frac{1}{D} \mathbf{1}\mathbf{1}^{\top}$ , and we arrive at

$$\mathcal{K} \approx \hat{\mathcal{K}}_{HD} \equiv \frac{\eta}{B} \sum_{\alpha=1}^D \frac{\lambda_{\alpha}}{2 - \eta\lambda_{\alpha}}\tag{11}$$

where the  $\lambda_{\alpha}$  are the eigenvalues of  $\hat{\Theta}$ . The key features are the dependence on the ratio  $\eta/B$ , and the fact that eigenvalues close to the deterministic EOS  $\eta\lambda = 2$  have higher weight. We can immediately see that the S-EOS condition is not vacuous; if the largest  $B$  eigenvalues have  $\eta\lambda = 1$ , then  $\mathcal{K} \geq 1$  while  $\eta\lambda_{max} < 2$ .

If  $\eta\lambda_{\alpha} \ll 2$  for all eigenvalues, we have the approximation

$$\mathcal{K} \approx \hat{\mathcal{K}}_{tr} \equiv \frac{\eta}{2B} \text{tr}(\hat{\Theta})\tag{12}$$

In this regime  $\mathcal{K}$  is the normalized trace of the empirical NTK  $\hat{\Theta}$ .

These approximations underestimate the noise level; we have  $\hat{\mathcal{K}}_{tr} \leq \hat{\mathcal{K}}_{HD} \leq \mathcal{K}$ . In general  $\hat{\mathcal{K}}_{tr}$  becomes a poor predictor of  $\mathcal{K}$  when there are eigenvalues close to  $2/\eta$ .  $\hat{\mathcal{K}}_{HD}$  loses accuracy when there is a large spread of eigenvalues. Both become inaccurate when the eigenvectors  $\mathbf{V}$  of  $\hat{\Theta}$  are no longer delocalized with respect to the coordinate basis of  $\mathbf{z}$ ; this is also the case where the off-diagonal effects are important and  $\mathcal{K}$  becomes a less accurate representation of the dynamics of the full  $\mathbf{T}$ . See Appendix A.4 for more details.

Regardless,  $\mathcal{K}$  and its approximations are accurate enough to estimate the effect of noise on optimization trajectories in a linear regression setting. In particular they are accurate enough that we can use them to study the deep learning setting, where models are non-linear. In Section 5 we provide experimental evidence that  $\mathcal{K}$  and the S-EOS are useful for understanding aspects of training deep neural networks.

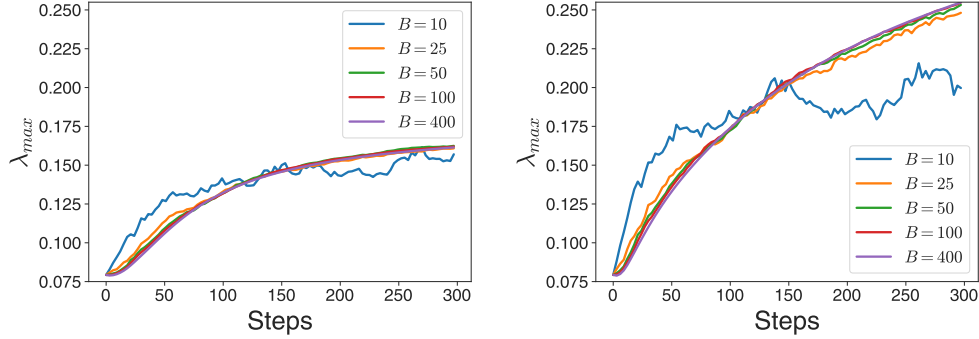


Figure 2: Dynamics of largest Hessian eigenvalue in quadratic regression model for fixed learning rate, various batch sizes. Small batch size leads to increased initial sharpening, but faster saturation (left, i.i.d.  $\mathbf{Q}$ ). Batch size differences are amplified when  $\mathbf{Q}$  is more heavily weighted in larger eigenmodes (right,  $V(\sigma) = \sigma$ ).

## 4 Conservative sharpening

In this section, we analyze *conservative sharpening* - the suppression of Hessian eigenvalue increase with decreasing batch size. We will provide theoretical evidence that SGD noise suppresses larger eigenvalues more than smaller ones. This phenomenology can help explain conditions under which the S-EOS can be reached in non-convex settings.

### 4.1 Quadratic regression model dynamics

We study the dynamics of the singular values of  $\mathbf{J}$  (and therefore the eigenvalues of  $\hat{\Theta}$ ) at early times in the quadratic regression model of Equation 5. We will model  $\mathbf{z}$  at initialization as i.i.d. random and independent of  $\mathbf{J}$  and  $\mathbf{Q}$ . We will model  $\mathbf{Q}$  as a random tensor to try to understand the eigenvalue dynamics in a “generic” situation without many assumptions. We will average over the randomness of  $\mathbf{Q}$ , with the idea that this can capture aspects of the behavior for large dataset size  $D$  and number of parameters  $P$ , where self-averaging may occur.

It has been previously observed that the model curvature tensor  $\mathbf{Q}$  has more “weight” in directions corresponding to the large NTK eigenvalues (Agarwala et al., 2022). Therefore we will define  $\mathbf{Q}$  using a tensor product decomposition. Let  $\mathbf{w}_\alpha$  be the left singular vector of  $\mathbf{J}_0$  associated with singular value  $\sigma_\alpha$ . Then we can decompose  $\mathbf{Q}$  as:

$$\mathbf{Q} = \sum_{\alpha} \mathbf{w}_\alpha \otimes \mathbf{M}_\alpha \quad (13)$$

where each  $\mathbf{M}_\alpha$  is a random  $P \times P$  symmetric matrix with i.i.d. elements with mean 0 and variance  $V(\sigma_\alpha)$ , for some non-decreasing function  $V$ . Note that  $V(\sigma) = 1$  is equivalent to an i.i.d. initialization of each element of  $\mathbf{Q}$ .

Numerically, we observe that for  $V(\sigma) = 1$ , for small batch sizes the largest eigenvalue increases more quickly than the full batch case, but its growth slows down quicker (Figure 2, left). However, if  $\mathbf{Q}$  is weighted more towards larger eigenmodes, as it is in practice, there is a more extreme deviation - even faster initial growth, but very strong suppression of future growth (Figure 2, right,  $V(\sigma) = \sigma$ ). This suggests that conservative sharpening depends on not just batch size, but the spectrum of  $\mathbf{Q}$  as well. We will prove these statements quantitatively in the quadratic regression model setting.

### 4.2 Estimating eigenvalue dynamics under SGD

In order to understand the eigenvalue dynamics, we will assume that the eigenvectors of the NTK change relatively slowly. This has been shown empirically for the large eigendirection of the Hessian (Bao et al., 2023), which correlate with the large NTK eigendirections (which are of particular interest here). Consider the following estimators. Let  $\{(\mathbf{w}_\alpha, \mathbf{v}_\alpha, \sigma_\alpha)\}$  be the set of triples that consists of a pair of the left and right singular vectors of  $\mathbf{J}_0$  associated with singular value  $\sigma_\alpha$ . We define the

equivalent approximate singular value  $\hat{\sigma}_{\alpha,t}$  and NTK eigenvalue  $\hat{\lambda}_{\alpha,t}$  as

$$\hat{\sigma}_{\alpha,t} \equiv \mathbf{w}_\alpha^\top \mathbf{J}_t \mathbf{v}_\alpha, \quad \hat{\lambda}_{\alpha,t} \equiv \mathbf{w}_\alpha^\top \mathbf{J}_t \mathbf{J}_t^\top \mathbf{w}_\alpha \quad (14)$$

Note that  $\hat{\sigma}_{\alpha,0}^2 = \hat{\lambda}_{\alpha,0} = \sigma_\alpha^2$ . If the singular vectors change slowly, then this lets us approximate the eigenvalues.

We will also compute the *discrete time derivatives*; for any timeseries  $\{x_t\}$  we write

$$\Delta_1 x_t \equiv x_{t+1} - x_t, \quad \Delta_2 x_t \equiv x_{t+2} - 2x_{t+1} + x_t. \quad (15)$$

We will show that the discrete first derivative increases with batch size while the discrete second derivative decreases with batch size, dependent on  $\sigma_\alpha$  and  $V(\sigma_\alpha)$ .

Concretely, we prove the following theorem (Appendix B):

**Theorem 4.1.** *Let  $\{(\mathbf{w}_\alpha, \mathbf{v}_\alpha, \sigma_\alpha)\}$  be the triple of left and right singular vectors of  $\mathbf{J}_0$  with the associated singular value. Let  $\mathbf{Q}$  be a random tensor with the decomposition given by Equation 13. Let  $\mathbf{z}_0$  have i.i.d. elements with mean 0 and variance  $V_z$ . If  $\mathbf{z}$ ,  $\mathbf{J}$ , and  $\mathbf{Q}$  are statistically independent, we can compute the following average discrete time derivatives (Equation 15) of the estimators  $\hat{\sigma}_0$  and  $\hat{\lambda}_0$  (Equation 14):*

$$\begin{aligned} \mathbb{E}_{\mathbf{P}, \mathbf{Q}, \mathbf{z}}[\Delta_1 \hat{\lambda}_{\alpha,0}] &= \\ B^{-1} P V_z \text{tr} \left[ \hat{\Theta}_t \right] \eta^2 V(\sigma_\alpha) + O(D^{-1}) \end{aligned} \quad (16)$$

$$\begin{aligned} \mathbb{E}_{\mathbf{P}, \mathbf{Q}, \mathbf{z}}[\Delta_2 \hat{\sigma}_{\alpha,0}] &= d_2(\eta) \\ &\quad - B^{-1} D^{-2} \eta^3 \sigma_{\alpha,t}^3 V(\sigma_\alpha) P V_z + O(\eta^4) \end{aligned} \quad (17)$$

where  $d_2(\tilde{\eta}) = \mathbb{E}_{\mathbf{P}, \mathbf{Q}, \mathbf{z}}[\Delta_2 \hat{\sigma}_{\alpha,0}]$  for  $\beta = 1$  and  $\eta = \tilde{\eta}$ .

For small batch size  $B$ , the first derivative is positive. This depends on the projection  $V(\sigma_\alpha)$ , but the average eigenvalue of  $\hat{\Theta}$ . In contrast, the second derivative is smaller (and indeed, can be negative) for smaller  $B$ , but depends on the particular singular value  $\sigma_\alpha^3$ . This suggests that the deviations due to SGD are more pronounced for eigenmodes with larger model curvature  $\mathbf{Q}$ , but also that conservative sharpening is stronger for larger eigenmodes.

It is the interplay between the spectra of  $\mathbf{J}$  and  $\mathbf{Q}$ , along with the batch size  $B$ , which determines the extend of conservative sharpening. Since the non-linear models in deep learning tend to have strong model curvature in large eigendirections, conservative sharpening can drive systems away from the deterministic EOS while leaving the S-EOS attainable - as we will see in the next section.

## 5 Experiments on neural networks

We conducted experimental studies on neural networks to understand how the noise kernel norm  $\mathcal{K}$  behaves in the convex setting. We will show that for small batch sizes,  $\mathcal{K}$  is a more informative object to study than  $\lambda_{max}$ , the key measurement in the full batch setting. We provide evidence that there is stabilization near the S-EOS, but unlike the deterministic EOS, the best training outcomes come from settings where  $\mathcal{K}$  is somewhat below the S-EOS.

### 5.1 Fully connected network, vanilla SGD

We begin by training a fully connected network on 2500 examples of MNIST with MSE loss. The details of the setup can be found in Appendix C. In this setting we can compute  $\mathcal{K}$  exactly and efficiently. We trained with a variety of batch sizes  $B$  and learning rates  $\eta$  to probe the dependence of learning dynamics on each of these hyperparameters.

Plotting training loss trajectories for fixed, small  $B$  and varying  $\eta$  elucidates some of the key phenomenology (Figure 3, left, for  $B = 1$ ). For very small  $\eta$ , the loss decreases smoothly but slowly. For larger  $\eta$ , the optimization is more efficient, and similar over a range of learning rates. Finally, for larger learning rates, the loss decreases slowly, until for the largest learning rates the loss diverges.

These different regimes are reflected in the dynamics of  $\mathcal{K}$  as well (Figure 3, right). At small  $\eta$ ,  $\mathcal{K}$  is small. This corresponds to a low noise regime where the steps are being taken conservatively.

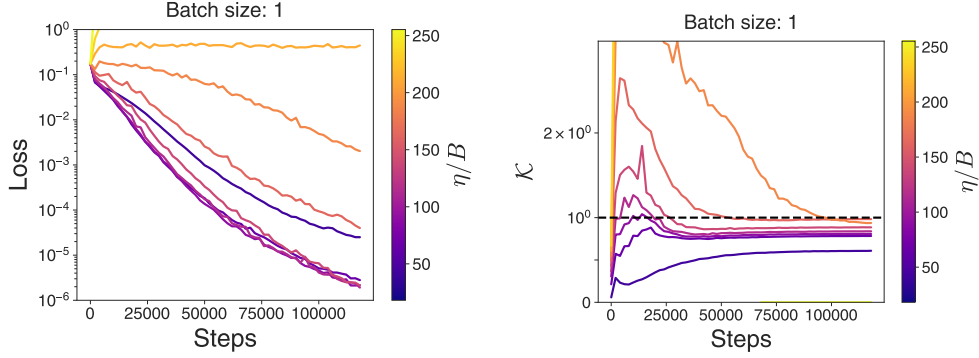


Figure 3: Dynamics of loss (left) and noise kernel norm  $\mathcal{K}$  (right) for a FCN trained on MNIST, various learning rates, batch size 1. For small learning rates, loss decrease is slow and kernel norm is well below 1. For intermediate learning rates,  $\mathcal{K}$  is larger than the critical value of 1, but then decreases and stabilizes below 1 and loss decreases quickly. For larger learning rates,  $\mathcal{K}$  stays above 1 for a long period and loss decreases slowly.

As  $\eta$  increases, we begin to see the emergence of S-EOS stabilization -  $\mathcal{K}$  is initially increasing, attains values above the S-EOS boundary  $\mathcal{K} = 1$ , but eventually stabilizes below 1. For the poorly optimizing trajectories at large  $\eta$ ,  $\mathcal{K}$  stays above 1 for a longer time.

These experiments suggest that there is a negative feedback effect which prevents the runaway growth of  $\mathcal{K}$  at intermediate  $\eta$ , and eventually drives it below the critical threshold. However, unlike the deterministic EOS, the S-EOS involves only a single, long time return to the critical value - unlike the period 2 quasi-stable oscillations around the boundary which characterize the deterministic EOS phase (Agarwala et al., 2022; Damian et al., 2022). Also, unlike the deterministic EOS, it is overall detrimental to stay very close to the S-EOS for long periods of time. This is due to the fact that the deterministic EOS involves only one eigenmode of  $\hat{\Theta}$  oscillating, while the others converge. In contrast, the S-EOS involves all the eigenmodes of  $\hat{\Theta}$  simultaneously due to coupling. In high dimensions this is the slow Malthusian exponent regime studied in Paquette et al. (2021).

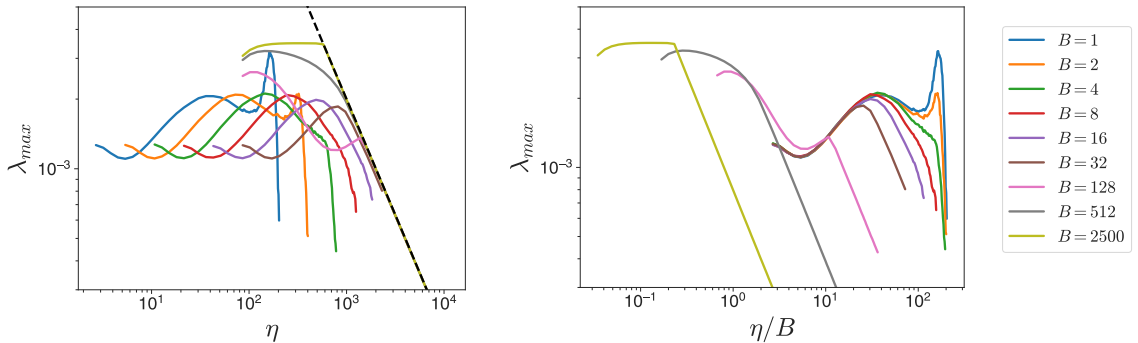


Figure 4:  $\lambda_{max}$  at convergence in MNIST experiment. Left: for large  $B$ , final values of  $\lambda_{max}$  are similar for same  $\eta$ , especially when dynamics reaches EOS as  $2/\eta$  (black dashed line); for small  $B$ ,  $\eta$  is not predictive of  $\lambda_{max}$  and EOS is not reached. Right: quantities are similar for equal  $\eta/B$  for small  $B$  and small  $\eta/B$ .

We also studied the dynamics of the largest NTK eigenvalue  $\lambda_{max}$  as a function of batch size and learning rate. For larger batch sizes, the final value of  $\lambda_{max}$  stabilizes at the deterministic EOS,  $2/\eta$ , over a wide range of learning rates (Figure 4, left). In this regime  $\eta$  alone sets the scale of  $\lambda_{max}$  independent of batch size. However, for small batch sizes, the dynamics diverges before the deterministic EOS is reached, and  $\eta$  alone is a poor predictor of the final  $\lambda_{max}$ . In this regime, it is more informative to plot the dynamics as a function of  $\eta/B$  (Figure 4, right). All batch sizes follow



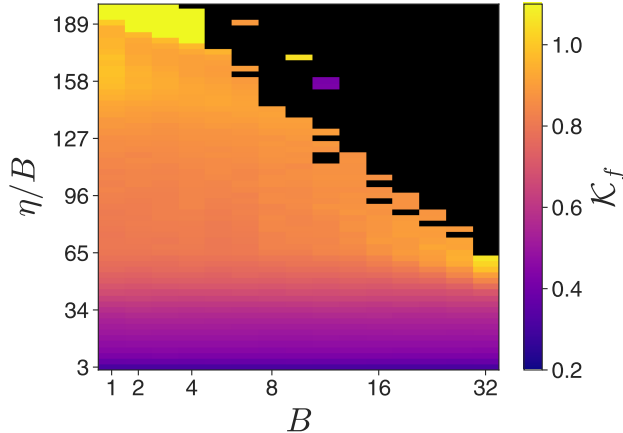


Figure 5: Final noise kernel norm  $\mathcal{K}_f$  after training for a fixed number of epochs with varying  $B$  and  $\eta$ . Value attained is well-predicted by  $\eta/B$  for various  $B$ . For fixed  $B$ ,  $\mathcal{K}_f$  increases with  $\eta$ , and attains a value near 1 over a significant range of learning rates, before training diverges at large learning rates. Divergence point comes at smaller  $\eta/B$  for larger  $B$ .

the  $B = 1$  curve for small and intermediate  $\eta/B$ , but there are batch-size dependent effects for larger learning rates.

For small  $B$ , it is more informative to study the final value of the noise kernel norm  $\mathcal{K}_f$  after a fixed number of epochs of training (Figure 5, 480 epochs). For small values of  $\eta/B$ ,  $\mathcal{K}_f$  is small, as expected, and there is consistent behavior across  $B$  for constant  $\eta/B$ . As  $\eta/B$  increases, there is a regime where the kernel norm takes on values in the range  $[0.7, 0.9]$  over a large range of learning rates. In this regime, there is consistency across constant  $\eta/B$ , over a limited range in  $B$  - dynamics for larger  $B$  now diverge.

In the small batch regime,  $\mathcal{K}_f$  is also highly informative of the final training loss reached (Figure 6, left). If  $\mathcal{K}_f$  is small, the dynamics has low noise but doesn't get as far in the given number of epochs. If  $\mathcal{K}_f$  is too close to 1, convergence also seems to slow down. In this setting there appears to be a good "intermediate zone" of  $\mathcal{K}_f \in [0.6, 0.8]$  where the learning rate is aggressive enough to drive the loss down considerably, but not enough to cause noise-induced convergence issues. In contrast, the maximum eigenvalue is a poor predictor of the final loss, even when scaled by the learning rate (Figure 6, right).

## 5.2 Momentum and learning rate schedule

In the MNIST example,  $\mathcal{K}$  could be computed exactly; what happens when this becomes intractable, due to model or dataset size? And what happens when things like momentum and learning rate schedule are thrown into the mix?

In order to probe these questions, we ran experiments on ResNet-18 trained on CIFAR10, with MSE loss, trained with momentum and cosine learning rate decay. The experimental details can be found in Appendix D. Computing  $\mathcal{K}$  now requires analysis of a  $5 \cdot 10^4 \times 5 \cdot 10^4$  dimensional matrix, whose elements are also expensive to compute (even using implicit matrix-vector product methods).

We instead used the trace approximation to  $\mathcal{K}$  discussed in Section 3.4. We computed additional corrections due to momentum and the  $L^2$  regularizer (see Appendices A.5 and A.6 for details). The value of the regularizer used in our experiments was small, and we arrived at the estimator

$$\hat{\mathcal{K}}_{mom} \equiv \frac{\eta}{2\alpha B} \text{tr} \left[ \hat{\Theta} \right] \quad (18)$$

where the momentum parameter  $\mu = 1 - \alpha$ . In all our experiments,  $\alpha = 0.1$ .

We trained over a variety of learning rates and batch sizes. We focus primarily on batch size 128 here; results for other batch sizes are similar and can be found in Appendix D. We found that the estimator  $\hat{\mathcal{K}}_{mom}$  starts low, increases dramatically at early times, levels off for much of training,

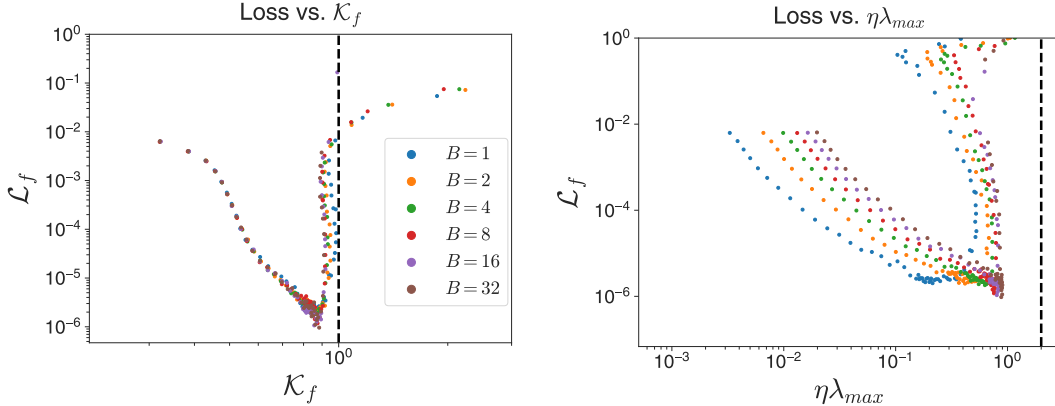


Figure 6: Final loss versus final noise kernel norm  $\mathcal{K}_f$  for fixed epoch training, various  $\eta$  and  $B$ .  $\mathcal{K}_f$  is a good predictor of final loss (left). Best training is for intermediate values of  $\mathcal{K}$  - small  $\mathcal{K}$  means stepsize is too conservative, large  $\mathcal{K}$  leads to slow convergence. In contrast,  $\lambda_{max}$  is a poor predictor of final loss (right). Dashed lines represent S-EOS (left) and EOS (right)

and then decreases at late times (Figure 7, left). It remains  $O(1)$  over a factor of 100 variation of the base learning rate. The decrease at late times is primarily due to the learning rate schedule; the unnormalized NTK trace is in fact slowly increasing for most of the trajectory (Figure 7, middle). We can also see the importance of the theoretical derivation of  $\mathcal{K}$ ; the normalized Hessian trace is not in fact  $O(1)$  and is completely dominated by the  $L^2$  regularizer and follows the cosine schedule (Figure 7, right). Even when removing the regularizer the non-GN part of the Hessian dominates the trace away from convergence, and the estimator is poor (Appendix D.4).

Even with learning rate schedules,  $\mathcal{K}$  can be a useful tool to understand aspects of learning dynamics. At large learning rates where  $\hat{\mathcal{K}}$  is near 1 for much of training, the test error decreases only slowly at that intermediate stage, before dropping quickly at late times where the schedule pushes  $\hat{\mathcal{K}}$  low (Figure 8, left, red curve). In contrast for a trajectory with low learning rate, the decrease is more smooth but still slower overall (blue curve). The intermediate learning rates with lowest test error also correspond to a median  $\hat{\mathcal{K}}$  value in the range  $[0.4, 0.8]$  (Figure 8, right).

We repeated the experiments on an MLP-Mixer S/16 architecture and found similar results to ResNet; see Appendix D.5 for more details.

## 6 Discussion

Our theoretical analysis and experiments suggest that there indeed is a stochastic edge of stability, which can be derived simply at least in the case of MSE loss. This S-EOS phenomenon displays non-linear stabilization of small instabilities, but seems to only stabilize once rather than the period 2 quasi-stable cycles of the deterministic version. Additionally, it appears that the best learning outcomes occur near but not at the S-EOS, due in part to the fact that the S-EOS phenomenon is acting across all the eigenmodes rather than just the top one.

The approximate form of  $\mathcal{K}$  in Equation 12 scales as  $\eta/B$ , which is in accordance with both SDE-based analyses of SGD (Smith et al., 2017; Jastrzebski et al., 2018), as well as practical observations of the “linear scaling rule” regime where scaling learning rate proportional to batch size achieves good performance (Goyal et al., 2018). Our constant-epoch experiments on the MNIST example suggest that there may be a link between the breakdown of the universal scaling regime of  $\mathcal{K}$  and the breakdown of the “perfect scaling” regime of steps to target scaling as  $B^{-1}$  in constant epoch experiments (Shallue et al., 2019).

One great advantage of the definition of  $\mathcal{K}$  is the fact that it is scaled properly independent of model and dataset size. In the convex, high dimensional, and homogeneous setting Paquette et al. (2021) showed that  $\mathcal{K}$  is exactly the quantity which controls convergence of the noise process. Our experiments suggest that even in the non-convex setting it is still meaningful. Previous works have

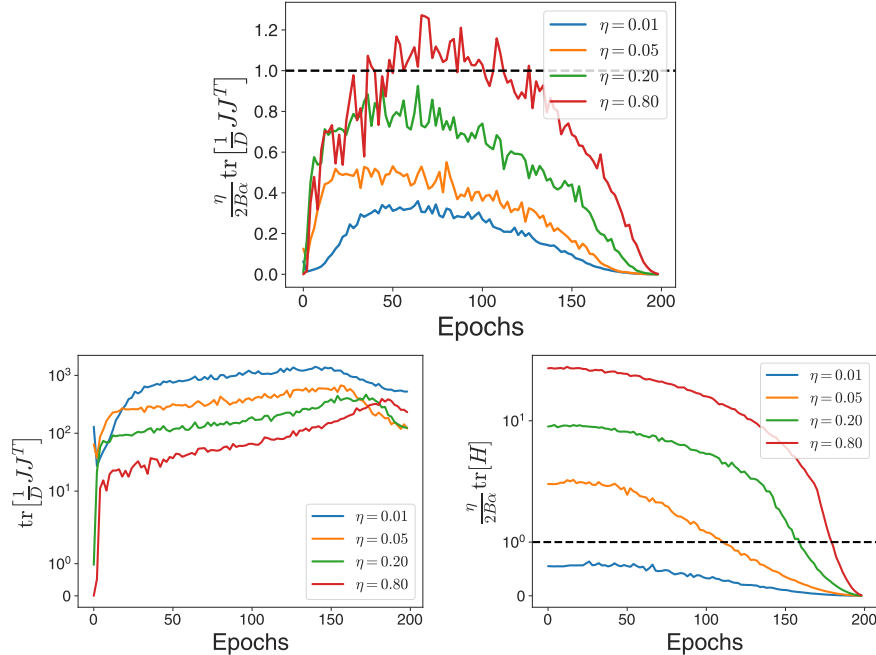


Figure 7: Estimates of kernel norm for ResNet-18 trained on CIFAR10 with momentum and cosine learning rate decay. Estimator based on NTK trace is initially increasing, becomes flat, and then decays while staying  $O(1)$  for a large range of  $\eta$  (top). Un-normalized quantity is increasing for much of learning but decreases at the end (bottom left). Normalized Hessian trace is dominated by  $L^2$  regularizer coefficient and largely follows learning rate schedule and is not well-normalized (bottom right).

used information from the Gauss Newton part of the Hessian (Wu & Su, 2023), which in high dimensions is equivalent to the NTK information. Their motivation was to analyze interpolating minima where the gradients of the loss with respect to the logits are close to 0; our analysis instead naturally reveals the NTK as the key player. In addition, our approach admits multiple tractable avenues to approximation of  $\mathcal{K}$ . The full Hessian suffers from sensitivity to  $L^2$  regularization, and the NME (non-Gauss Newton part of the Hessian) is known to have non-trivial trace when the number of parameters is large (Dauphin et al., 2024).

Another interesting result of our experiments is the observation that  $\mathcal{K}$  is, at least in certain cases, a good predictor of training outcomes. Our theoretical analysis focuses entirely on training dynamics and optimization, but even this is important in the compute limited regimes where large models are often trained. Our CIFAR experiments also suggest that there may be links between the dynamics of  $\mathcal{K}$  and generalization, but establishing this would require additional theory and experimental work.

Both the definition of  $\mathcal{K}$  and the analysis of conservative sharpening suggest that in order to understand SGD dynamics, one must understand the *distribution* of NTK/Hessian eigenvalues. In fact our analysis of conservative sharpening suggests that the distribution of *model curvatures* is also crucial in understanding how the loss landscape geometry evolves in SGD.

## 7 Future directions

One key future direction is to extend some of the analyses to more general loss functions and optimizers. For example the definition of  $\mathcal{K}$  can be adapted for any loss near a minimum that admits a Taylor series expansion; however, much of the interesting training dynamics occurs far from minima. There are already promising approaches to general loss functions in limited high dimensional settings, e.g. (Collins-Woodfin et al., 2023) which may provide a way forward.

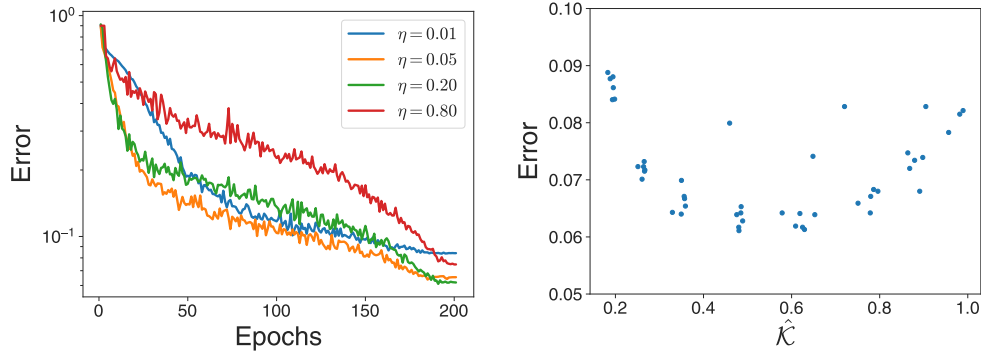


Figure 8: Error for various base learning rates, ResNet-18 trained on CIFAR10. Small base learning rate shows slower initial and late time error improvements, while large learning rate shows slow early time error improvements (left). Best error is achieved for settings where median  $\mathcal{K}$  remains within the interval  $[0.4, 0.8]$  (right).

Another extension is to develop algorithms that either control or use  $\mathcal{K}$ . Algorithms like SAM (Foret et al., 2022) have been developed to control directions of larger curvature, and control all eigenmodes even away from minima (Agarwala & Dauphin, 2023); however, there may be better ways to control the average rather than largest eigenvalue. A greater understanding of conservative sharpening may lead to other ways to control the statistics of the Hessian.

Maybe the most interesting direction is the prospect of using information about  $\mathcal{K}$  to dynamically choose step sizes. Traditional step size tuning methods often fail dramatically in deep learning (Roulet et al., 2023), and some of that failure may be due to not incorporating information relevant to SGD. This will require further refining estimators of  $\mathcal{K}$  or equivalents so the statistics can be updated efficiently and frequently enough to be useful.

## 8 Impact statement

This paper presents work whose goal is to advance the field of Machine Learning. There are many potential societal consequences of our work, none which we feel must be specifically highlighted here.

## References

- Adlam, B. and Pennington, J. The Neural Tangent Kernel in High Dimensions: Triple Descent and a Multi-Scale Theory of Generalization. In *Proceedings of the 37th International Conference on Machine Learning*, pp. 74–84. PMLR, November 2020.
- Agarwala, A. and Dauphin, Y. SAM operates far from home: Eigenvalue regularization as a dynamical phenomenon. In *Proceedings of the 40th International Conference on Machine Learning*, pp. 152–168. PMLR, July 2023.
- Agarwala, A., Pedregosa, F., and Pennington, J. Second-order regression models exhibit progressive sharpening to the edge of stability, October 2022.
- Arnaboldi, L., Stephan, L., Krzakala, F., and Loureiro, B. From high-dimensional & mean-field dynamics to dimensionless ODEs: A unifying approach to SGD in two-layers networks, February 2023.
- Bao, X., Bietti, A., Defazio, A., and Cabannes, V. Hessian Inertia in Neural Networks. *1st Workshop on High-dimensional Learning Dynamics, ICML, 2023*.
- Ben Arous, G., Gheissari, R., and Jagannath, A. High-dimensional limit theorems for SGD: Effective dynamics and critical scaling. *Advances in Neural Information Processing Systems*, 35:25349–25362, December 2022.

- Cohen, J., Kaur, S., Li, Y., Kolter, J. Z., and Talwalkar, A. Gradient Descent on Neural Networks Typically Occurs at the Edge of Stability. In *International Conference on Learning Representations*, February 2022a.
- Cohen, J. M., Ghorbani, B., Krishnan, S., Agarwal, N., Medapati, S., Badura, M., Suo, D., Cardoze, D., Nado, Z., Dahl, G. E., and Gilmer, J. Adaptive Gradient Methods at the Edge of Stability, July 2022b.
- Collins-Woodfin, E., Paquette, C., Paquette, E., and Seroussi, I. Hitting the High-Dimensional Notes: An ODE for SGD learning dynamics on GLMs and multi-index models, August 2023.
- Damian, A., Nichani, E., and Lee, J. D. Self-Stabilization: The Implicit Bias of Gradient Descent at the Edge of Stability, September 2022.
- Dauphin, Y. N., Agarwala, A., and Mobahi, H. Neglected Hessian component explains mysteries in Sharpness regularization, January 2024.
- Foret, P., Kleiner, A., Mobahi, H., and Neyshabur, B. Sharpness-aware Minimization for Efficiently Improving Generalization. In *International Conference on Learning Representations*, April 2022.
- Ghorbani, B., Krishnan, S., and Xiao, Y. An Investigation into Neural Net Optimization via Hessian Eigenvalue Density. In *Proceedings of the 36th International Conference on Machine Learning*, pp. 2232–2241. PMLR, May 2019.
- Gilmer, J., Ghorbani, B., Garg, A., Kudugunta, S., Neyshabur, B., Cardoze, D., Dahl, G. E., Nado, Z., and Firat, O. A Loss Curvature Perspective on Training Instabilities of Deep Learning Models. In *International Conference on Learning Representations*, March 2022.
- Goyal, P., Dollár, P., Girshick, R., Noordhuis, P., Wesolowski, L., Kyrola, A., Tulloch, A., Jia, Y., and He, K. Accurate, Large Minibatch SGD: Training ImageNet in 1 Hour, April 2018.
- He, K., Zhang, X., Ren, S., and Sun, J. Deep Residual Learning for Image Recognition. In *Proceedings of the IEEE Conference on Computer Vision and Pattern Recognition*, pp. 770–778, 2016.
- Jacot, A., Gabriel, F., and Hongler, C. Neural Tangent Kernel: Convergence and Generalization in Neural Networks. In *Advances in Neural Information Processing Systems 31*, pp. 8571–8580. Curran Associates, Inc., 2018.
- Jastrzebski, S., Szymczak, M., Fort, S., Arpit, D., Tabor, J., Cho, K., and Geras, K. The Break-Even Point on Optimization Trajectories of Deep Neural Networks, February 2020.
- Jastrzebski, S., Kenton, Z., Arpit, D., Ballas, N., Fischer, A., Bengio, Y., and Storkey, A. Three Factors Influencing Minima in SGD, September 2018.
- Lee, J., Xiao, L., Schoenholz, S., Bahri, Y., Novak, R., Sohl-Dickstein, J., and Pennington, J. Wide Neural Networks of Any Depth Evolve as Linear Models Under Gradient Descent. In *Advances in Neural Information Processing Systems 32*, pp. 8570–8581. Curran Associates, Inc., 2019.
- Ma, C. and Ying, L. On Linear Stability of SGD and Input-Smoothness of Neural Networks. In *Advances in Neural Information Processing Systems*, volume 34, pp. 16805–16817. Curran Associates, Inc., 2021.
- Mei, S., Misiakiewicz, T., and Montanari, A. Mean-field theory of two-layers neural networks: Dimension-free bounds and kernel limit. In *Proceedings of the Thirty-Second Conference on Learning Theory*, pp. 2388–2464. PMLR, June 2019.
- Mulayoff, R. and Michaeli, T. Exact Mean Square Linear Stability Analysis for SGD, June 2023.
- Paquette, C., Lee, K., Pedregosa, F., and Paquette, E. SGD in the Large: Average-case Analysis, Asymptotics, and Stepsize Criticality. In *Proceedings of Thirty Fourth Conference on Learning Theory*, pp. 3548–3626. PMLR, July 2021.
- Paquette, C., Paquette, E., Adlam, B., and Pennington, J. Homogenization of SGD in high-dimensions: Exact dynamics and generalization properties, May 2022a.

- Paquette, C., Paquette, E., Adlam, B., and Pennington, J. Implicit Regularization or Implicit Conditioning? Exact Risk Trajectories of SGD in High Dimensions, June 2022b.
- Roulet, V., Agarwala, A., and Pedregosa, F. On the Interplay Between Stepsize Tuning and Progressive Sharpening, December 2023.
- Shallue, C. J., Lee, J., Antognini, J., Sohl-Dickstein, J., Frostig, R., and Dahl, G. E. Measuring the Effects of Data Parallelism on Neural Network Training. *Journal of Machine Learning Research*, 20(112):1–49, 2019. ISSN 1533-7928.
- Smith, S. L., Kindermans, P.-J., and Le, Q. V. Don’t Decay the Learning Rate, Increase the Batch Size. *arXiv preprint arXiv:1711.00489*, 2017.
- Tolstikhin, I., Houlsby, N., Kolesnikov, A., Beyer, L., Zhai, X., Unterthiner, T., Yung, J., Steiner, A., Keysers, D., Uszkoreit, J., Lucic, M., and Dosovitskiy, A. MLP-Mixer: An all-MLP Architecture for Vision, June 2021.
- Wu, L. and Su, W. J. The Implicit Regularization of Dynamical Stability in Stochastic Gradient Descent. In *Proceedings of the 40th International Conference on Machine Learning*, pp. 37656–37684. PMLR, July 2023.
- Wu, L., Wang, M., and Su, W. The alignment property of SGD noise and how it helps select flat minima: A stability analysis, October 2022.
- Zhu, L., Liu, C., Radhakrishnan, A., and Belkin, M. Quadratic models for understanding neural network dynamics, May 2022.

## A Stochastic edge of stability

### A.1 Averaging lemma

Here we prove a lemma which is used to take second moments with respect to SGD noise. Recall that  $\mathbf{P}_t$  is a sequence of i.i.d. random diagonal  $D \times D$  matrices with  $B$  1s and  $D - B$  0s on the diagonal. We have the following lemma:

**Lemma A.1.** *Let  $\mathbf{M}$  be a matrix independent of  $\mathbf{P}_t$  for all  $t$ . Then we have the following moments:*

$$\begin{aligned} \mathbb{E}[\mathbf{P}_t] &= \beta \mathbf{I}, \quad \mathbb{E}[\mathbf{P}_t \mathbf{M} \mathbf{P}_{t+1}] = \beta^2 \mathbf{M} \\ \mathbb{E}[\mathbf{P}_t \mathbf{M} \mathbf{P}_t] &= \beta \tilde{\beta} \mathbf{M} + \beta(1 - \tilde{\beta}) \text{diag}(\mathbf{M}) \end{aligned} \quad (19)$$

where  $\beta \equiv B/D$  and  $\tilde{\beta} \equiv (B - 1)/(D - 1)$ .

*Proof.* The first moment of  $\mathbf{P}_t$  is derived by averaging each diagonal term. Similarly,  $\mathbb{E}[\mathbf{P}_t \mathbf{M} \mathbf{P}_{t+1}] = \mathbb{E}[\mathbf{P}_t] \mathbf{M} \mathbb{E}[\mathbf{P}_{t+1}]$  since  $\mathbf{P}_t$  and  $\mathbf{P}_{t+1}$  are independent.

Now consider  $\mathbb{E}[\mathbf{P}_t \mathbf{M} \mathbf{P}_t]$ . There are two cases to consider. First, consider the diagonal of the output. For a coordinate  $\alpha$  we have:

$$[\mathbf{P}_t \mathbf{M} \mathbf{P}_t]_{\alpha\alpha} = [\mathbf{P}_t]_{\alpha\alpha} [\mathbf{M}]_{\alpha\alpha} [\mathbf{P}_t]_{\alpha\alpha} = \begin{cases} [\mathbf{M}]_{\alpha\alpha} & \text{with probability } \beta \\ 0 & \text{with probability } (1 - \beta) \end{cases} \quad (20)$$

That is, the  $\alpha\alpha$  diagonal element is non-zero precisely when the  $\alpha\alpha$  diagonal element of  $\mathbf{P}$  is non-zero.

In the off-diagonal case, the  $\alpha\beta$  element with  $\alpha \neq \beta$  gives us:

$$[\mathbf{P}_t \mathbf{M} \mathbf{P}_t]_{\alpha\beta} = [\mathbf{P}_t]_{\alpha\alpha} [\mathbf{M}]_{\alpha\beta} [\mathbf{P}_t]_{\alpha\beta} = \begin{cases} [\mathbf{M}]_{\alpha\beta} & \text{with probability } \binom{B-2}{D-2} / \binom{B}{D} \\ 0 & \text{with probability } 1 - \binom{B-2}{D-2} / \binom{B}{D} \end{cases} \quad (21)$$

Here the element is non-zero if and only if both  $\alpha$  and  $\beta$  are selected in the batch.

Taken together, in coordinates we can write:

$$\mathbb{E}[\mathbf{P}_t \mathbf{M} \mathbf{P}_t]_{\alpha\beta} = \frac{B}{D} [\delta_{\alpha\beta} + (B - 1)/(D - 1)(1 - \delta_{\alpha\beta})] \mathbf{M}_{\alpha\beta} \quad (22)$$

$$\mathbb{E}[\mathbf{P}_t \mathbf{M} \mathbf{P}_t]_{\alpha\beta} = \beta [\delta_{\alpha\beta} + \tilde{\beta}(1 - \delta_{\alpha\beta})] \mathbf{M}_{\alpha\beta} \quad (23)$$

Writing in matrix notation, we have the desired result.  $\square$

### A.2 Derivation of second moment dynamics

Here we derive the various dynamical equations for the second moment of  $\mathbf{z}$  in the linear model. We begin by noting that:

$$\mathbb{E}_{\mathbf{P}}[\mathbf{z}_{t+1} \mathbf{z}_{t+1}^\top - \mathbf{z}_t \mathbf{z}_t^\top | \mathbf{z}_t] = \mathbf{z}_t \mathbb{E}_{\mathbf{P}}[\mathbf{z}_{t+1} - \mathbf{z}_t | \mathbf{z}_t]^\top + \mathbb{E}_{\mathbf{P}}[\mathbf{z}_{t+1} - \mathbf{z}_t | \mathbf{z}_t] \mathbf{z}_t^\top + \mathbb{E}_{\mathbf{P}}[(\mathbf{z}_{t+1} - \mathbf{z}_t)(\mathbf{z}_{t+1} - \mathbf{z}_t)^\top | \mathbf{z}_t] \quad (24)$$

Substitution gives us:

$$\mathbb{E}_{\mathbf{P}}[\mathbf{z}_{t+1} \mathbf{z}_{t+1}^\top - \mathbf{z}_t \mathbf{z}_t^\top | \mathbf{z}_t] = -\frac{\eta}{B} (\mathbf{z}_t \mathbb{E}_{\mathbf{P}}[\mathbf{z}_t^\top \mathbf{P}_t \mathbf{J} \mathbf{J}^\top] + \mathbb{E}_{\mathbf{P}}[\mathbf{J} \mathbf{J}^\top \mathbf{P}_t \mathbf{z}_t] \mathbf{z}_t^\top) + \frac{\eta^2}{B^2} \mathbb{E}_{\mathbf{P}}[\mathbf{J} \mathbf{J}^\top \mathbf{P}_t \mathbf{z}_t \mathbf{z}_t^\top \mathbf{P}_t \mathbf{J} \mathbf{J}^\top] \quad (25)$$

Evaluation using Lemma A.1 gives us

$$\mathbb{E}_{\mathbf{P}}[\mathbf{z}_{t+1} \mathbf{z}_{t+1}^\top | \mathbf{z}_t] = \mathbf{z}_t \mathbf{z}_t^\top - \eta \left( \hat{\Theta} \mathbf{z}_t \mathbf{z}_t^\top + \mathbf{z}_t \mathbf{z}_t^\top \hat{\Theta} \right) + \tilde{\beta} \beta^{-1} \eta^2 \hat{\Theta} \mathbf{z}_t \mathbf{z}_t^\top \hat{\Theta} + \left( \beta^{-1} - \tilde{\beta} \beta^{-1} \right) \eta^2 \hat{\Theta} \text{diag}[\mathbf{z}_t \mathbf{z}_t^\top] \hat{\Theta} \quad (26)$$

This means that  $\mathbb{E}_{\mathbf{P}}[\mathbf{z}_t \mathbf{z}_t^\top]$  evolves according to a linear dynamical system. We denote the linear operator defining the dynamics as  $\mathbf{T}$ .

We can rotate to the eigenbasis of the NTK. Given the eigendecomposition  $\hat{\Theta} = \mathbf{V}\mathbf{\Lambda}\mathbf{V}^\top$ , we define the matrix  $\mathbf{S}_t$  as:

$$\mathbf{S}_t \equiv \mathbf{V}^\top \mathbb{E}_{\mathcal{P}}[\mathbf{z}_t \mathbf{z}_t^\top] \mathbf{V} \quad (27)$$

The diagonal elements of  $\mathbf{S}_t$  correspond to the squared eigenprojections  $\mathbb{E}_{\mathcal{P}}[(\mathbf{v}_\alpha \cdot \mathbf{z}_t)^2]$ , while the off-diagonal elements correspond to correlations  $\mathbb{E}_{\mathcal{P}}[(\mathbf{v}_\alpha \cdot \mathbf{z}_t)(\mathbf{v}_\beta \cdot \mathbf{z}_t)]$ .

$\mathbf{S}_t$  also evolves linearly, according to the dynamical system:

$$\mathbb{E}[\mathbf{S}_{t+1} | \mathbf{z}_t] = \mathbf{S}_t - \eta(\mathbf{\Lambda}\mathbf{S}_t + \mathbf{S}_t\mathbf{\Lambda}) + \tilde{\beta}\beta^{-1}\eta^2\mathbf{\Lambda}\mathbf{S}_t\mathbf{\Lambda} + (\beta^{-1} - \tilde{\beta}\beta^{-1})\eta^2\mathbf{\Lambda}\mathbf{V}^\top \left[ \sum_{\alpha} (\mathbf{V}\mathbf{S}_t\mathbf{V}^\top)_{\alpha\alpha} \mathbf{e}_\alpha \mathbf{e}_\alpha^\top \right] \mathbf{V}\mathbf{\Lambda} \quad (28)$$

where  $\mathbf{e}_\alpha$  is the basis element for coordinate  $\alpha$  in the original coordinate system. The last term induces coupling in between the different elements of  $\mathbf{S}_t$  - that is, between the covariances of the different eigenmodes of  $\hat{\Theta}$ . In coordinates we have:

$$[\mathbf{\Lambda}\mathbf{V}^\top \text{diag}[\mathbf{V}\mathbf{S}_t\mathbf{V}^\top] \mathbf{V}\mathbf{\Lambda}]_{\mu\nu} = \lambda_\mu \lambda_\nu \left[ \sum_{\alpha} \mathbf{V}_{\alpha\beta} \mathbf{V}_{\alpha\gamma} \mathbf{V}_{\alpha\mu} \mathbf{V}_{\alpha\nu} \right] (\mathbf{S}_t)_{\beta\gamma} \quad (29)$$

That is, there is non-zero coupling between the residual dynamics in the eigendirections of  $\hat{\Theta}$ , and potentially non-trivial contributions from the covariances between different modes. This is an effect entirely driven by SGD noise, as in the deterministic case the eigenmodes of  $\hat{\Theta}$  evolve independently.

We can write the operator  $\mathbf{T}$  in the  $\mathbf{S}$  basis, using a 4-index notation:

$$\mathbf{T}_{\mu\nu, \beta\gamma} = \delta_{\mu\beta, \nu\gamma} (1 - \eta(\lambda_\mu + \lambda_\nu) + \tilde{\beta}\beta^{-1}\eta^2\lambda_\mu\lambda_\nu) + (\beta^{-1} - \tilde{\beta}\beta^{-1})\eta^2\lambda_\mu\lambda_\nu \left[ \sum_{\alpha} \mathbf{V}_{\alpha\beta} \mathbf{V}_{\alpha\gamma} \mathbf{V}_{\alpha\mu} \mathbf{V}_{\alpha\nu} \right] \quad (30)$$

In this notation,  $(\mathbf{S}_{t+1})_{\mu\nu} = \sum_{\beta\gamma} \mathbf{T}_{\mu\nu, \beta\gamma} (\mathbf{S}_t)_{\beta\gamma}$ .

In the main text, we analyzed the dynamics restricted to the diagonal of  $\mathbf{S}$ . Let  $\mathbf{p} \equiv \text{diag}(\mathbf{S})$ . The dynamical equation is, coordinate-wise:

$$(\mathbf{p}_{t+1})_\mu = \sum_{\beta} \mathbf{T}_{\mu\mu, \beta\beta} (\mathbf{p}_t)_\beta \quad (31)$$

which becomes, in matrix notation

$$\mathbf{p}_{t+1} = \mathbf{D}\mathbf{p}_t, \quad \mathbf{D} \equiv [(\mathbf{I} - \eta\mathbf{\Lambda})^2 + (\tilde{\beta}\beta^{-1} - 1)\eta^2\mathbf{\Lambda}^2 + \eta^2(\beta^{-1} - \tilde{\beta}\beta^{-1})\mathbf{\Lambda}^2\mathbf{C}], \quad \mathbf{C}_{\beta\mu} \equiv \sum_{\alpha} \mathbf{V}_{\alpha\beta}^2 \mathbf{V}_{\alpha\mu}^2 \quad (32)$$

Note that  $\mathbf{C}$  is a PSD (and indeed, non-negative) matrix. If  $\mathbf{\Lambda}$  is invertible,  $\mathbf{D}$  has all real non-negative eigenvalues, as seen via similarity transformation (left multiply by  $\mathbf{\Lambda}^{-1}$ , right multiply by  $\mathbf{\Lambda}$ ). In the general case, if we define  $\tilde{\mathbf{p}} = \mathbf{\Lambda}^\dagger \mathbf{p}$  (transformation by the Moore-Penrose pseudoinverse of  $\mathbf{\Lambda}$ ), we have:

$$\tilde{\mathbf{p}}_{t+1} = [(\mathbf{I} - \eta\mathbf{\Lambda})^2 + (\tilde{\beta}\beta^{-1} - 1)\eta^2\mathbf{\Lambda}^2 + \eta^2(\beta^{-1} - 1)\mathbf{\Lambda}\mathbf{C}\mathbf{\Lambda}] \tilde{\mathbf{p}}_t \quad (33)$$

This leads us directly to the decomposition in Equation 9.

### A.3 Proof of Theorem 3.1

We will use the following lemmas:

**Lemma A.2.** *Let  $a$  and  $b$  be random variables with finite first and second moment. Then  $\mathbb{E}[|ab|] \leq \mathbb{E}[a^2] + \mathbb{E}[b^2]$ .*

*Proof.* Given any fixed  $a$  and  $b$ ,  $|ab| \leq a^2 + b^2$ . From the linearity of expectation we have the desired result.  $\square$

**Lemma A.3.** *Let  $\mathbf{A}$  and  $\mathbf{B}$  be two PSD matrices. Then*

$$\max \lambda[\mathbf{A}] \leq \max \lambda[\mathbf{A} + \mathbf{B}] \quad (34)$$



*Proof.* Let  $\mathbf{v}$  be an eigenvector of  $\mathbf{A}$  associated with the largest eigenvalue, with length 1. Then we have:

$$\mathbf{v}^\top [\mathbf{A} + \mathbf{B}] \mathbf{v} = \max \lambda[\mathbf{A}] + \mathbf{v}^\top \mathbf{B} \mathbf{v} \geq \max \lambda[\mathbf{A}] \quad (35)$$

where the final inequality comes from the PSDness of  $\mathbf{B}$ . Note that  $\mathbf{A} + \mathbf{B}$  is PSD since  $\mathbf{A}$  and  $\mathbf{B}$  are individually. Therefore, we have

$$\mathbf{v}^\top [\mathbf{A} + \mathbf{B}] \mathbf{v} = \sum_k (\mathbf{v} \cdot \mathbf{w}_k)^2 \lambda_k \quad (36)$$

where  $\mathbf{w}_k$  is the eigenvector of  $\mathbf{A} + \mathbf{B}$  associated with the eigenvalue  $\lambda_k$ . Since the  $\lambda_k$  are non-negative, and the  $(\mathbf{v} \cdot \mathbf{w}_k)^2$  are non-negative and sum to 1, we have

$$\mathbf{v}^\top [\mathbf{A} + \mathbf{B}] \mathbf{v} \leq \max \lambda[\mathbf{A} + \mathbf{B}] \quad (37)$$

Combining all our inequalities, we have:

$$\max \lambda[\mathbf{A}] \leq \max \lambda[\mathbf{A} + \mathbf{B}] \quad (38)$$

□

**Lemma A.4.** *Let  $\mathbf{A}$  and  $\mathbf{B}$  be PSD matrices. Then the product  $\mathbf{A}\mathbf{B}$  has non-negative eigenvalues.*

*Proof.* Consider the symmetric matrix  $\mathbf{M} = (\mathbf{B})^{1/2} \mathbf{A} \mathbf{B}^{1/2}$ . This matrix is PSD since

$$\mathbf{w}^\top (\mathbf{B})^{1/2} \mathbf{A} \mathbf{B}^{1/2} \mathbf{w} = [(\mathbf{B})^{1/2} \mathbf{w}]^\top \mathbf{A} [(\mathbf{B})^{1/2} \mathbf{w}] \geq 0 \quad (39)$$

for any  $\mathbf{w}$ , by the PSDness of  $\mathbf{A}$ . Let  $\mathbf{v}$  be an eigenvector of  $\mathbf{B}^{1/2} \mathbf{A} \mathbf{B}^{1/2}$  associated with eigenvalue  $\lambda$ . We consider two cases. The first is that  $\mathbf{B}^{1/2} \mathbf{v} = 0$ . In this case,  $\mathbf{A} \mathbf{B} \mathbf{v} = 0$ , and  $\mathbf{v}$  is an eigenvector of eigenvalue 0 for  $\mathbf{A} \mathbf{B}$  as well.

Now we consider non-zero eigenvalues of  $\mathbf{M}$ . WLOG we choose a basis such that the eigenvalue condition for positive  $\lambda$  can be written as

$$\mathbf{M} \begin{pmatrix} \mathbf{v} \\ 0 \end{pmatrix} = \begin{pmatrix} \mathbf{L} & 0 \\ 0 & 0 \end{pmatrix} \begin{pmatrix} \mathbf{A}_{11} & \mathbf{A}_{12} \\ \mathbf{A}_{21} & \mathbf{A}_{22} \end{pmatrix} \begin{pmatrix} \mathbf{L} & 0 \\ 0 & 0 \end{pmatrix} \begin{pmatrix} \mathbf{v} \\ 0 \end{pmatrix} = \lambda \begin{pmatrix} \mathbf{v} \\ 0 \end{pmatrix} \quad (40)$$

where  $\mathbf{L}$  is a positive diagonal matrix. Now consider the following product involving  $\mathbf{A}\mathbf{B}$ :

$$\mathbf{A}\mathbf{B} \begin{pmatrix} \mathbf{L}^{-1} \mathbf{v} \\ \mathbf{u} \end{pmatrix} = \begin{pmatrix} \mathbf{A}_{11} & \mathbf{A}_{12} \\ \mathbf{A}_{21} & \mathbf{A}_{22} \end{pmatrix} \begin{pmatrix} \mathbf{L}^2 & 0 \\ 0 & 0 \end{pmatrix} \begin{pmatrix} \mathbf{L}^{-1} \mathbf{v} \\ \mathbf{u} \end{pmatrix} \quad (41)$$

We can rewrite this as

$$\mathbf{A}\mathbf{B} \begin{pmatrix} \mathbf{L}^{-1} \mathbf{v} \\ \mathbf{u} \end{pmatrix} = \begin{pmatrix} \mathbf{L}^{-1} & 0 \\ 0 & \mathbf{I} \end{pmatrix} \begin{pmatrix} \mathbf{L} & 0 \\ 0 & \mathbf{I} \end{pmatrix} \begin{pmatrix} \mathbf{A}_{11} & \mathbf{A}_{12} \\ \mathbf{A}_{21} & \mathbf{A}_{22} \end{pmatrix} \begin{pmatrix} \mathbf{L}^2 & 0 \\ 0 & 0 \end{pmatrix} \begin{pmatrix} \mathbf{v} \\ \mathbf{u} \end{pmatrix} \quad (42)$$

Using the eigenvalue condition we have:

$$\mathbf{A}\mathbf{B} \begin{pmatrix} \mathbf{L}^{-1} \mathbf{v} \\ \mathbf{u} \end{pmatrix} = \begin{pmatrix} \lambda \mathbf{L}^{-1} \mathbf{v} \\ \mathbf{A}_{21} \mathbf{v} \end{pmatrix} \quad (43)$$

If we select  $\mathbf{u} = \lambda^{-1} \mathbf{A}_{21} \mathbf{v}$ , then we have

$$\mathbf{A}\mathbf{B} \begin{pmatrix} \mathbf{L}^{-1} \mathbf{v} \\ \mathbf{u} \end{pmatrix} = \lambda \begin{pmatrix} \mathbf{L}^{-1} \mathbf{v} \\ \mathbf{u} \end{pmatrix} \quad (44)$$

Therefore  $\lambda$  is an eigenvalue of  $\mathbf{A}\mathbf{B}$ . All eigenvalues of  $\mathbf{A}\mathbf{B}$  are non-negative. □

Lemmas in hand, we can now prove the theorem. A key point is that the theorem would be trivial if  $\mathbf{A}$  and  $\mathbf{B}$  were scalars; in this case, it would be equivalent to  $A < 1$ ,  $A + B < 1$  if and only if  $(1 - A)^{-1} B < 1$ . We will use the PSD nature of  $\mathbf{A}$  and  $\mathbf{B}$  to extend the trivial manipulation of scalar inequalities to their linear algebraic counterparts in terms of the largest eigenvalues of the corresponding matrices.

**Theorem 3.1** Given the dynamics of Equation 9,  $\lim_{t \rightarrow \infty} \mathbb{E}_{\mathcal{P}}[\mathbf{z}_t \mathbf{z}_t^\top] = 0$  for any initialization  $\mathbf{z}_t$  if and only if  $\|\mathbf{A}\|_{op} < 1$  and  $\mathcal{K} < 1$  where

$$\mathcal{K} \equiv \max \lambda [(\mathbf{I} - \mathbf{A})^{-1} \mathbf{B}] \quad (45)$$

for the PSD matrices  $\mathbf{A}$  and  $\mathbf{B}$  defined above.  $\mathcal{K}$  is always non-negative.

*Proof.* We begin with Equation 9. This is a linear dynamical system which determines the values of  $\mathbb{E}_{\mathcal{P}}[\text{diag}(\mathbf{z}_t \mathbf{z}_t^\top)]$ . From Lemma A.2,  $\lim_{t \rightarrow \infty} \mathbb{E}_{\mathcal{P}}[\text{diag}(\mathbf{z}_t \mathbf{z}_t^\top)]$  implies  $\lim_{t \rightarrow \infty} \mathbb{E}_{\mathcal{P}}[\mathbf{z}_t \mathbf{z}_t^\top]$  for off-diagonal elements as well.

The linear system converges to 0 for all inputs if and only if  $L_{max}$ , the largest eigenvalue of  $\mathbf{A} + \mathbf{B}$ , has absolute value less than 1. Since  $\mathbf{A}$  and  $\mathbf{B}$  are both PSD, this condition is equivalent to  $L_{max} < 1$ . From Lemma A.3 we have:

$$\|\mathbf{A}\|_{op} = \max \lambda[\mathbf{A}] \leq \max \lambda[\mathbf{A} + \mathbf{B}] \quad (46)$$

Therefore, if  $\|\mathbf{A}\|_{op} \geq 1$ ,  $L_{max} \geq 1$  and the dynamics does not converge to 0.

Now consider the case  $\|\mathbf{A}\|_{op} < 1$ . We first show that  $\max \lambda[(\mathbf{I} - \mathbf{A})^{-1} \mathbf{B}] \geq 1$  implies  $\max \lambda[\mathbf{A} + \mathbf{B}] \geq 1$ . Since  $\|\mathbf{A}\|_{op} < 1$ ,  $\mathbf{I} - \mathbf{A}$  is invertible. Let  $\mathbf{w}$  be an eigenvector of  $(\mathbf{I} - \mathbf{A})^{-1} \mathbf{B}$  with eigenvalue  $\omega \geq 1$ . Then:

$$\mathbf{w}^\top \mathbf{B} \mathbf{w} = \mathbf{w}^\top (\mathbf{I} - \mathbf{A})(\mathbf{I} - \mathbf{A})^{-1} \mathbf{B} \mathbf{w} = \omega \mathbf{w}^\top (\mathbf{I} - \mathbf{A}) \mathbf{w} \quad (47)$$

This implies that

$$\mathbf{w}^\top [\mathbf{A} + \mathbf{B}] \mathbf{w} = \omega \mathbf{w}^\top \mathbf{I} \mathbf{w} + (1 - \omega) \mathbf{w}^\top \mathbf{A} \mathbf{w} \quad (48)$$

Since  $\|\mathbf{A}\|_{op} < 1$ ,  $(1 - \omega) \mathbf{w}^\top \mathbf{A} \mathbf{w} \geq 1 - \omega$  and we have

$$\mathbf{w}^\top [\mathbf{A} + \mathbf{B}] \mathbf{w} \geq \omega + (1 - \omega) = 1 \quad (49)$$

Therefore,  $\max \lambda[\mathbf{A} + \mathbf{B}] \geq 1$  and  $\lim_{t \rightarrow \infty} \mathbb{E}_t[\mathbf{z}_t \mathbf{z}_t^\top] \neq 0$  for all initializations.

Now we show the converse. Suppose  $\max \lambda[\mathbf{A} + \mathbf{B}] \geq 1$ . Let  $\mathbf{u}$  be an eigenvector of  $\mathbf{A} + \mathbf{B}$  with eigenvalue  $\nu > 1$ . We note that the symmetric matrix  $(\mathbf{I} - \mathbf{A})^{-1/2} \mathbf{B} (\mathbf{I} - \mathbf{A})^{-1/2}$  has the same spectrum as  $(\mathbf{I} - \mathbf{A})^{-1} \mathbf{B}$ . Let  $\tilde{\mathbf{u}} \equiv (\mathbf{I} - \mathbf{A})^{1/2} \mathbf{u}$ . We have:

$$\frac{\tilde{\mathbf{u}}^\top (\mathbf{I} - \mathbf{A})^{-1/2} \mathbf{B} (\mathbf{I} - \mathbf{A})^{-1/2} \tilde{\mathbf{u}}}{\tilde{\mathbf{u}}^\top \tilde{\mathbf{u}}} = \frac{\mathbf{u}^\top \mathbf{B} \mathbf{u}}{\mathbf{u}^\top (\mathbf{I} - \mathbf{A}) \mathbf{u}} = \frac{\mathbf{u}^\top (\nu \mathbf{I} - \mathbf{A}) \mathbf{u}}{\mathbf{u}^\top (\mathbf{I} - \mathbf{A}) \mathbf{u}} = 1 + \frac{\nu - 1}{\mathbf{u}^\top (\mathbf{I} - \mathbf{A}) \mathbf{u}} \quad (50)$$

Since  $\nu > 1$  and  $\mathbf{I} - \mathbf{A}$  is PSD and invertible,  $\mathbf{u}^\top (\mathbf{I} - \mathbf{A}) \mathbf{u} > 0$ . Therefore, the expression is greater than 0. This means that  $\max \lambda[(\mathbf{I} - \mathbf{A})^{-1/2} \mathbf{B} (\mathbf{I} - \mathbf{A})^{-1/2}] \geq 1$ , and accordingly  $\max \lambda[(\mathbf{I} - \mathbf{A})^{-1} \mathbf{B}] \geq 1$

Note that  $\max \lambda[(\mathbf{I} - \mathbf{A})^{-1} \mathbf{B}]$  is always non-negative by Lemma A.4. This concludes the proof.  $\square$

#### A.4 Validity of $\mathcal{K}$ and approximations

The analysis of Paquette et al. (2021) established the following approximation for  $\mathcal{K}$ :

$$\mathcal{K} \approx \hat{\mathcal{K}}_{HD} = \frac{\eta}{B} \sum_{\alpha=1}^D \frac{\lambda_\alpha}{2 - \eta \lambda_\alpha} \quad (51)$$

This approximation holds in the limit of large  $D$ , with sufficiently smooth convergence of the spectrum of  $\frac{1}{D} \mathbf{J} \mathbf{J}^\top$  to its limiting distribution, and a rotational invariance assumption on the distribution of eigenvectors in the limit. For  $\eta \lambda \ll 2$ , there is an even simpler approximator:

$$\mathcal{K} \approx \hat{\mathcal{K}}_{tr} = \frac{\eta}{B} \text{tr}[\hat{\Theta}] \quad (52)$$

We can compare the approximations to  $\mathcal{K}$  in different settings, and in turn compare  $\mathcal{K}$  to the exact  $\max \|\lambda[\mathbf{T}]\|$ . We performed numerical experiments in 3 settings ( $D = 100$ ,  $P = 120$ ,  $B = 5$ ):

- **Flat spectrum.** Here  $\mathbf{J}$  was chosen to have i.i.d. elements, and the resulting spectrum limits to Marchenko-Pastur in the high dimensional limit. This is the setting where  $\mathcal{K}$  and its approximations best capture  $\max \|\lambda[\mathbf{T}]\|$ .
- **Dispersed spectrum.** Here we chose a spectrum  $\lambda_\alpha = 1/(\alpha^2 + 1)$  for the NTK, where the eigenvectors of  $\hat{\Theta}$  were chosen from a rotationally invariant distribution. This causes  $\hat{\mathcal{K}}_{tr}$  to differ from  $\hat{\mathcal{K}}_{HD}$  and  $\hat{\mathcal{K}}_{HD}$  differs from  $\mathcal{K}$ , but  $\mathcal{K}$  still approximates  $\max \|\lambda[\mathbf{T}]\|$ .
- **Localized eigenvectors.** Here  $\hat{\Theta} = \text{diag}(|\mathbf{s}|) + \frac{1}{D}\mathbf{J}_0\mathbf{J}_0^\top$  for a vector  $\mathbf{s}$  drawn i.i.d. from a Gaussian with  $\sigma = 0.1$ , and  $\mathbf{J}_0$  from an i.i.d. Gaussian. This causes  $\hat{\Theta}$  to have additional weight on the diagonal, and causes the eigenvectors to delocalize in the coordinate basis. This is the most “adversarial” setup for the approximation scheme, and  $\mathcal{K}$  no longer predicts  $\max \|\lambda[\mathbf{T}]\|$  to high accuracy.

We can see the various stability measures as a function of  $\eta$  in Figure 9. As previously explained,  $\max \|\lambda[\mathbf{T}]\|$  takes a value close to 1 for small learning rates, until the S-EOS is reached and it rises above 1. In contrast,  $\mathcal{K}$  and its approximators start at 0 for small learning rate and approach 1 monotonically from below - by design. In all cases, the maximum eigenvalue is well below the edge of stability value of  $2/\eta$  (purple curve), so any instability is due to the S-EOS.

In the flat spectrum case (Figure 9, left),  $\mathcal{K}$  and its approximators all give good predictions of the S-EOS - or equivalently, the region of learning rates where  $\max \|\lambda[\mathbf{T}]\| > 1$ . In the dispersed spectrum setting (Figure 9, middle), the differences between the approximations are more apparent. However,  $\mathcal{K}$  still predicts the S-EOS.

Finally, in the localized eigenvectors case, even  $\mathcal{K}$  is a bad approximator of the S-EOS (Figure 9, right). The dynamics becomes unstable for values of  $\mathcal{K}$  well below 1. It is not surprising that  $\mathcal{K}$  does not capture the behavior of  $\max \|\lambda[\mathbf{T}]\|$  here. From the high dimensional analysis, we know that the effect of the noise term is to evenly couple the different eigenmodes of  $\hat{\Theta}$ ; this is possible because the eigenbasis of  $\hat{\Theta}$  has no correlation with the coordinate eigenbasis. Having eigenvectors correlated with the coordinate basis breaks this property and leads to the approximations leading to  $\mathcal{K}$  to become bad.

The differences between the setups can be made even more clear by looking at the loss at late times, as a function of the stability measures (Figure 10, for  $10^4$  steps). We see that  $\max \|\lambda[\mathbf{T}]\| = 1$  predicts the transition from convergent to divergent well in all settings,  $\mathcal{K} = 1$  predicts it well in all but the localized eigenvectors setting, and  $\hat{\mathcal{K}}_{HD}$  already starts to become inaccurate in the dispersed setting.

This analysis suggests that  $\hat{\mathcal{K}}_{HD}$  and  $\hat{\mathcal{K}}_{tr}$  are conservative estimators of the noise level, but that  $\mathcal{K}$  itself is a good estimator of the S-EOS as long as the eigenvectors of  $\hat{\Theta}$  remain delocalized. The approximations tend to get better in high dimensions, but even in low dimensions they still provide valuable information on parameter ranges where the optimization enters the noise-dominated regime.

## A.5 $\mathcal{K}$ and momentum

In this section, we analyze the noise kernel norm with momentum.

In the high-dimensional isotropic case, we can compute  $\mathcal{K}$  for SGD with momentum. Consider momentum with parameter  $\mu$ , where the updates evolve as:

$$\mathbf{v}_{t+1} = \mu\mathbf{v}_t + \mathbf{g}_t \quad (53)$$

$$\boldsymbol{\theta}_{t+1} = \boldsymbol{\theta}_t + \eta\mathbf{v}_t \quad (54)$$

for gradient  $\mathbf{g}$ . In a linear model,

$$\mathbf{g}_t = -\mathbf{J}\mathbf{J}^\top\mathbf{P}_t\mathbf{z}_t \quad (55)$$

As per the analysis of Paquette et al. (2021), the second moment dynamics of  $\mathbf{z}$  close once again. In the high dimensional limit, where  $\mathbf{C} = \frac{1}{D}\mathbf{1}\mathbf{1}^\top$ , we get the noise kernel norm given by:

$$\mathcal{K} = \beta(1 - \beta)\frac{1}{D}\sum_{t=0}^{\infty}\sum_{\alpha=1}^D\frac{2\eta^2\lambda_\alpha^2}{\Omega_\alpha^2 - 4\mu}\left(\mu^{t+1} + \frac{1}{2}\nu_{+, \alpha}^{t+1} + \frac{1}{2}\nu_{-, \alpha}^{t+1}\right) \quad (56)$$

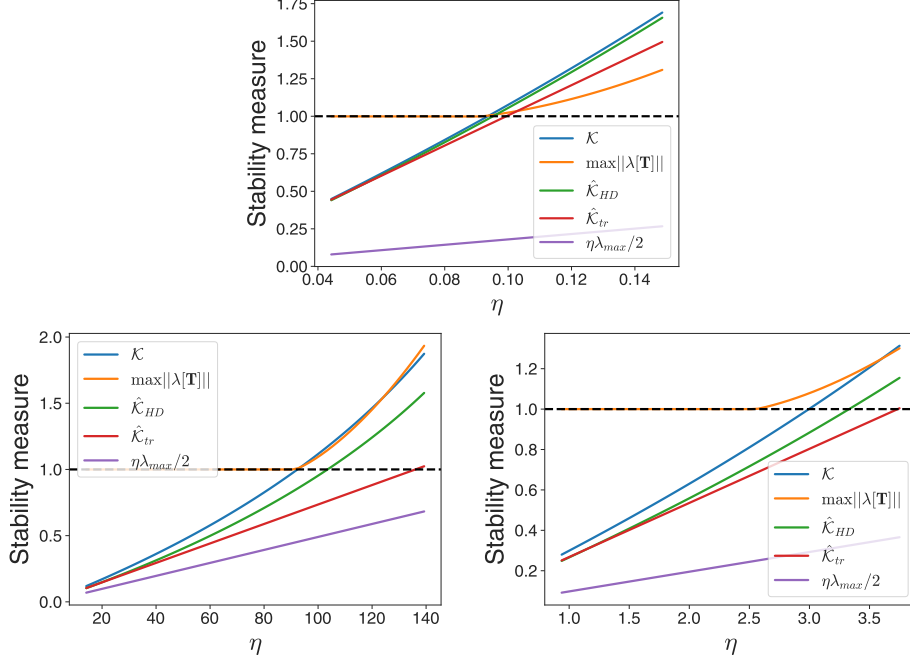


Figure 9: Stability measures for SGD in linear model with  $D = 100$ ,  $P = 120$ , and  $B = 5$ . For i.i.d. initialization of  $\mathbf{J}$ , NTK spectrum is not very varied and approximations are close to  $\mathcal{K}$  (top). However, in the case of dispersed spectra ( $\lambda_\alpha = 1/(\alpha^2 + 1)$ , bottom left), and localized eigenvectors (NTK  $\text{diag}(|\mathbf{s}|) + \frac{1}{D}\mathbf{J}_0\mathbf{J}_0^\top$ ,  $\mathbf{s}$  and  $\mathbf{J}_0$  i.i.d, bottom right) approximations are less accurate. In all cases, maximum eigenvalue is well below stability threshold (red curves).

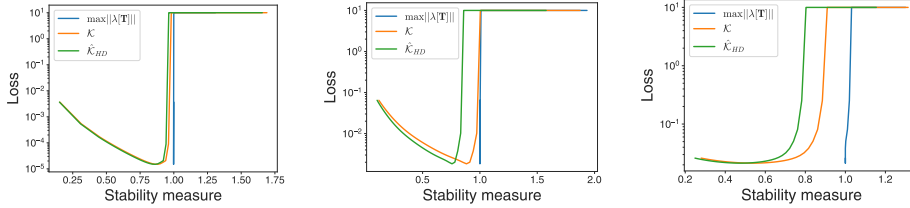


Figure 10: Loss versus stability measures after  $10^4$  steps, for flat spectrum, dispersed spectrum, and localized eigenvector settings. All curves saturated at loss value 10 for ease of plotting. With a flat spectrum (left), all three of  $\max \|\lambda[\mathbf{T}]\|$ ,  $\mathcal{K}$ , and  $\hat{\mathcal{K}}_{HD}$  predict divergence of loss at the critical value of 1. For dispersed spectrum,  $\mathcal{K}$  is still a good approximator of the convergent regime but  $\hat{\mathcal{K}}_{HD}$  is less so. For localized eigenvector setting, only  $\max \|\lambda[\mathbf{T}]\|$  predicts the transition.

where  $\Omega_\alpha = 1 - \beta\eta\lambda_\alpha + \mu$  and

$$\nu_{\alpha,\pm} = \frac{-2\mu + \Omega_\alpha^2 \pm \sqrt{\Omega_\alpha^2(\Omega_\alpha^2 - 4\mu)}}{2} \quad (57)$$

We can simplify this expression considerably. Carrying out the sum over  $t$  we have:

$$\mathcal{K} = \beta(1 - \beta) \frac{1}{D} \sum_{\alpha=1}^D \frac{2\eta^2\lambda_\alpha^2}{\Omega_\alpha^2 - 4\mu} \left( \frac{\mu}{1 - \mu} + \frac{1}{2} \left[ \frac{\nu_{+,\alpha}}{1 - \nu_{+,\alpha}} + \frac{\nu_{-,\alpha}}{1 - \nu_{-,\alpha}} \right] \right) \quad (58)$$

If we write  $\nu_{\alpha,\pm} = \frac{1}{2}(a \pm b)$ , we have:

$$\frac{\nu_{+,\alpha}}{1 - \nu_{+,\alpha}} + \frac{\nu_{-,\alpha}}{1 - \nu_{-,\alpha}} = \frac{a + b}{2 - (a + b)} + \frac{a - b}{2 - (a - b)} = \frac{(a - b)(2 - (a + b)) + (a + b)(2 - (a - b))}{4 - 4a + (a^2 - b^2)} \quad (59)$$

$$\frac{\nu_{+,\alpha}}{1-\nu_{+,\alpha}} + \frac{\nu_{-,\alpha}}{1-\nu_{-,\alpha}} = \frac{4a - 2(a^2 - b^2)}{4 - 4a + (a^2 - b^2)} \quad (60)$$

We have:

$$a^2 - b^2 = (-2\mu + \Omega_\alpha^2)^2 - (\Omega_\alpha^2(\Omega_\alpha^2 - 4\mu)) = 4\mu^2 \quad (61)$$

Simplification gives us

$$\frac{\nu_{+,\alpha}}{1-\nu_{+,\alpha}} + \frac{\nu_{-,\alpha}}{1-\nu_{-,\alpha}} = \frac{4(\Omega_\alpha^2 - 2\mu) - 8\mu^2}{4 - 4(\Omega_\alpha^2 - 2\mu) + 4\mu^2} = \frac{(\Omega_\alpha^2 - 2\mu) - 2\mu^2}{1 - (\Omega_\alpha^2 - 2\mu) + \mu^2} \quad (62)$$

$$\frac{\nu_{+,\alpha}}{1-\nu_{+,\alpha}} + \frac{\nu_{-,\alpha}}{1-\nu_{-,\alpha}} = \frac{\Omega_\alpha^2 - 2\mu - 2\mu^2}{-\Omega_\alpha^2 + (1 + \mu)^2} \quad (63)$$

Substituting  $\Omega_\alpha = 1 - \beta\eta\lambda_\alpha + \mu$ , we have:

$$\frac{\nu_{+,\alpha}}{1-\nu_{+,\alpha}} + \frac{\nu_{-,\alpha}}{1-\nu_{-,\alpha}} = \frac{(1 - \beta\eta\lambda_\alpha + \mu)^2 - 2\mu - 2\mu^2}{-(1 - \beta\eta\lambda_\alpha + \mu)^2 + (1 + \mu)^2} = \frac{(1 - \beta\eta\lambda_\alpha)^2 - 2\mu\beta\eta\lambda_\alpha - \mu^2}{2(1 + \mu)\beta\eta\lambda_\alpha - (\beta\eta\lambda_\alpha)^2} \quad (64)$$

The denominator of  $\mathcal{K}$  can be written as

$$\Omega_\alpha^2 - 4\mu = (1 - \beta\eta\lambda_\alpha + \mu)^2 - 4\mu = (1 - \mu)^2 - 2(1 + \mu)\beta\eta\lambda_\alpha + (\beta\eta\lambda_\alpha)^2 \quad (65)$$

Therefore we can re-write the noise kernel norm as:

$$\mathcal{K} = \frac{\beta(1-\beta)}{2D} \sum_{\alpha=1}^D \frac{2\eta^2\lambda_\alpha^2}{(1-\mu)^2 - 2(1+\mu)\beta\eta\lambda_\alpha + (\beta\eta\lambda_\alpha)^2} \left( -\frac{2\mu}{1-\mu} + \frac{(1-\beta\eta\lambda_\alpha)^2 - 2\mu\beta\eta\lambda_\alpha - \mu^2}{2(1+\mu)\beta\eta\lambda_\alpha - (\beta\eta\lambda_\alpha)^2} \right) \quad (66)$$

As a sanity check, for  $\mu = 0$  we have  $\Omega_\alpha = 1 - \beta\eta\lambda_\alpha$  and

$$\frac{\nu_{+,\alpha}}{1-\nu_{+,\alpha}} + \frac{\nu_{-,\alpha}}{1-\nu_{-,\alpha}} = \frac{(1 - \beta\eta\lambda_\alpha)^2}{2\beta\eta\lambda_\alpha - (\beta\eta\lambda_\alpha)^2} \quad (67)$$

which leads to

$$\mathcal{K} = \frac{\beta(1-\beta)}{2D} \sum_{\alpha=1}^D \frac{2\eta^2\lambda_\alpha^2}{(1-\beta\eta\lambda_\alpha)^2} \frac{(1-\beta\eta\lambda_\alpha)^2}{2\beta\eta\lambda_\alpha - (\beta\eta\lambda_\alpha)^2} = (1-\beta) \frac{1}{D} \sum_{\alpha=1}^D \frac{\eta\lambda_\alpha}{2-\beta\eta\lambda_\alpha} \quad (68)$$

as before.

If we re-write the momentum as  $\mu = 1 - \alpha$ , we have:

$$\frac{\nu_{+,\alpha}}{1-\nu_{+,\alpha}} + \frac{\nu_{-,\alpha}}{1-\nu_{-,\alpha}} = \frac{(1 - \beta\eta\lambda_\alpha)^2 - 2\beta\eta\lambda_\alpha + 2\alpha\beta\eta\lambda_\alpha - 1 + 2\alpha - \alpha^2}{2(2 - \alpha)\beta\eta\lambda_\alpha - (\beta\eta\lambda_\alpha)^2} \quad (69)$$

$$\frac{\nu_{+,\alpha}}{1-\nu_{+,\alpha}} + \frac{\nu_{-,\alpha}}{1-\nu_{-,\alpha}} = \frac{-4\beta\eta\lambda_\alpha + (\beta\eta\lambda_\alpha)^2 + 2\alpha(1 + \beta\eta\lambda_\alpha) - \alpha^2}{2(2 - \alpha)\beta\eta\lambda_\alpha - (\beta\eta\lambda_\alpha)^2} \quad (70)$$

This gives us the noise kernel norm:

$$\mathcal{K} = \frac{\beta(1-\beta)}{D} \sum_{\alpha=1}^D \frac{\eta^2\lambda_\alpha^2}{-2\beta\eta\lambda_\alpha + 2\alpha\beta\eta\lambda_\alpha + \alpha^2 + (\beta\eta\lambda_\alpha)^2} \left( -\frac{2(1-\alpha)}{\alpha} + \frac{-4\beta\eta\lambda_\alpha + (\beta\eta\lambda_\alpha)^2 + 2\alpha(1 + \beta\eta\lambda_\alpha) - \alpha^2}{2(2-\alpha)\beta\eta\lambda_\alpha - (\beta\eta\lambda_\alpha)^2} \right) \quad (71)$$

We have already simplified for no momentum ( $\alpha = 1$ ). Now we consider the opposite limit of  $\alpha \ll 1$ . We are also interested in  $\beta\eta\lambda_\alpha \ll 1$ . In order for the denominator (of each term in the  $t$  sum) to be non-negative, we take:  $\alpha \gg \sqrt{\beta\eta\lambda_\alpha}$ . To lowest order we have:

$$\mathcal{K} \approx \beta(1-\beta) \frac{1}{D} \sum_{\alpha=1}^D \frac{\eta^2\lambda_\alpha^2}{\alpha^2} \left( -\frac{2}{\alpha} + \frac{\alpha}{2\beta\eta\lambda_\alpha} \right) \quad (72)$$

which gives us

$$\mathcal{K} \approx \beta(1-\beta) \left[ -\frac{2}{D} \sum_{\alpha=1}^D \frac{\eta^2\lambda_\alpha^2}{\alpha^3} + \frac{1}{D} \sum_{\alpha=1}^D \frac{\eta\lambda_\alpha}{2\alpha\beta} \right] \quad (73)$$

If we perform the familiar conversions  $\lambda_\alpha = D\lambda_\alpha$  and  $\eta = \eta_0/B$ , we have:

$$\mathcal{K} \approx \left( \frac{1}{B} - \frac{1}{D} \right) \left[ \frac{1}{2\alpha} \sum_{\alpha=1}^D \eta_0 \lambda_\alpha - \frac{2}{\alpha^3} \sum_{\alpha=1}^D \eta_0^2 \lambda_\alpha^2 \right] \quad (74)$$

Note that  $\alpha^2 \gg \beta\eta\lambda_\alpha = B\eta\lambda_\alpha$ . Therefore,

$$\frac{1}{\alpha^3} \sum_{\alpha=1}^D \eta_0^2 \lambda_\alpha^2 \ll \frac{1}{\alpha} \frac{1}{B} \sum_{\alpha=1}^D \eta_0 \lambda_\alpha \quad (75)$$

At large batch size  $B$  the first term dominates and we have

$$\mathcal{K} \approx \frac{1}{2} \left( \frac{1}{B} - \frac{1}{D} \right) \sum_{\alpha=1}^D (\eta_0/\alpha) \lambda_\alpha \quad (76)$$

The lowest order correction is evidently to replace  $\eta_0$  with  $\eta_0/\alpha$ . The form of the corrections suggest that as  $\alpha$  increases ( $\mu$  decreasing from 1), the net effect is some extra stabilization relative to the effective learning rate  $\eta_0/\alpha$ .

### A.6 $\mathcal{K}$ and $L^2$ regularization

Consider  $L^2$  regularization in a linear model, with strength parameter  $\rho$ . The dynamical equation for  $\mathbf{z}$  becomes:

$$\mathbf{z}_{t+1} - \mathbf{z}_t = -\eta (\mathbf{J}\mathbf{J}^\top \mathbf{P}_t \mathbf{z}_t + \rho \mathbf{J}^\top \boldsymbol{\theta}_t) \quad (77)$$

This gives us

$$\mathbf{z}_{t+1} - \mathbf{z}_t = -\eta (\mathbf{J}\mathbf{J}^\top \mathbf{P}_t + \rho \mathbf{I}) \mathbf{z}_t \quad (78)$$

The covariance evolves as

$$\mathbf{z}_{t+1} \mathbf{z}_{t+1}^\top - \mathbf{z}_t \mathbf{z}_t^\top = -\eta (\mathbf{J}\mathbf{J}^\top \mathbf{P}_t + \rho \mathbf{I}) \mathbf{z}_t \mathbf{z}_t^\top - \eta \mathbf{z}_t \mathbf{z}_t^\top (\mathbf{J}\mathbf{J}^\top \mathbf{P}_t + \rho \mathbf{I}) + \eta^2 (\mathbf{J}\mathbf{J}^\top \mathbf{P}_t + \rho \mathbf{I}) \mathbf{z}_t \mathbf{z}_t^\top (\mathbf{J}\mathbf{J}^\top \mathbf{P}_t + \rho \mathbf{I}) \quad (79)$$

Averaging over  $\mathbf{P}$  once again, we have:

$$\begin{aligned} \mathbb{E}_{\mathbf{P}} [\mathbf{z}_{t+1} \mathbf{z}_{t+1}^\top - \mathbf{z}_t \mathbf{z}_t^\top] &= -\eta (\beta \mathbf{J}\mathbf{J}^\top + \rho \mathbf{I}) \mathbf{z}_t \mathbf{z}_t^\top - \eta \mathbf{z}_t \mathbf{z}_t^\top (\beta \mathbf{J}\mathbf{J}^\top + \rho \mathbf{I}) + \\ &\quad \eta^2 (\beta \mathbf{J}\mathbf{J}^\top + \rho \mathbf{I}) \mathbf{z}_t \mathbf{z}_t^\top (\beta \mathbf{J}\mathbf{J}^\top + \rho \mathbf{I}) + \beta(1-\beta)\eta^2 \mathbf{J}\mathbf{J}^\top \text{diag} [\mathbf{z}_t \mathbf{z}_t^\top] \mathbf{J}\mathbf{J}^\top \end{aligned} \quad (80)$$

If we once again define  $\mathbf{p}_t$  to be the vector with elements  $\mathbb{E}_{\mathbf{P}}[(\mathbf{v}_\alpha \cdot \mathbf{z}_t)^2]$ , where the  $\mathbf{v}_\alpha$  are the eigenvectors of  $\mathbf{J}\mathbf{J}^\top$ , we have

$$\mathbf{p}_t = \mathbf{D}^t \mathbf{p}_0, \quad \mathbf{D} \equiv (\mathbf{I} - \beta\eta\boldsymbol{\Lambda} - \eta\rho\mathbf{I})^2 + \beta(1-\beta)\eta^2 \boldsymbol{\Lambda}^2 \mathbf{C} \quad (81)$$

where  $\mathbf{C}$  is defined as before. In the high-dimensional limit, the noise kernel norm becomes

$$\|\mathcal{K}\| = \beta(1-\beta) \sum_{\alpha} \frac{\eta^2 \lambda_\alpha^2}{1 - (1 - \beta\eta\lambda_\alpha - \eta\rho)^2} \quad (82)$$

This is bounded from above by the  $\rho = 0$  case:

$$\beta(1-\beta) \sum_{\alpha} \frac{\eta^2 \lambda_\alpha^2}{1 - (1 - \beta\eta\lambda_\alpha - \eta\rho)^2} \leq \beta(1-\beta) \sum_{\alpha} \frac{\eta^2 \lambda_\alpha^2}{1 - (1 - \beta\eta\lambda_\alpha)^2} \quad (83)$$

Which suggests that the regularization decreases the noise kernel norm in this case.

Simplifying, we have:

$$\|\mathcal{K}\| = (\beta^{-1} - 1) \sum_{\alpha} \frac{\beta^2 \eta^2 \lambda_\alpha^2}{2(\beta\eta\lambda_\alpha + \eta\rho) - (\beta\eta\lambda_\alpha + \eta\rho)^2} \quad (84)$$

Dividing the numerator and denominator by  $\beta\eta\lambda_\alpha$ , we have

$$\|\mathcal{K}\| = (\beta^{-1} - 1) \sum_{\alpha} \frac{\beta\eta\lambda_\alpha}{2 - \beta\eta\lambda_\alpha + (\rho/\lambda_\alpha) - 2\eta\rho - \eta\rho^2/\lambda_\alpha} \quad (85)$$

We can look at limiting behaviors to see two different types of contributions. Assume  $\eta\rho \ll 1$ . We have:

$$\frac{\beta\eta\lambda_\alpha}{2 - \beta\eta\lambda_\alpha + (\rho/\lambda_\alpha) - 2\eta\rho - \eta\rho^2/\lambda_\alpha} \approx \begin{cases} \frac{\beta\eta\lambda_\alpha}{2 - \beta\eta\lambda_\alpha} & \text{if } \beta\eta\lambda_\alpha \gg \eta\rho \\ \frac{\beta\lambda_\alpha}{\rho} \frac{\beta\eta\lambda_\alpha}{2} & \text{if } \beta\eta\lambda_\alpha \ll \eta\rho \end{cases} \quad (86)$$

Evidently the effect of the normalization is to decrease the contribution of eigenvalues such that  $\beta\lambda_\alpha < \rho$ .

## B Conservative sharpening in the quadratic regression model

In this section, we prove Theorem 4.1 in two parts, and provide numerical evidence for its validity.

For ease of notation, we define  $\tilde{\eta} = \eta/B$ . This is equivalent to the scaling in Paquette et al. (2021), and allows us to keep the calculations in terms of  $\beta$  rather than the raw  $B$ . The final theorem can be obtained with the substitution of  $\tilde{\eta}$ .

### B.1 First discrete derivative of NTK

By definition we have

$$\Delta_1 \hat{\lambda}_{\alpha,t} = \mathbf{w}_\alpha^\top [\mathbf{J}_{t+1} \mathbf{J}_{t+1}^\top - \mathbf{J}_t \mathbf{J}_t^\top] \mathbf{w}_\alpha \quad (87)$$

Using Equation 5, and averaging over  $\mathbf{P}$  we have

$$\begin{aligned} \mathbb{E}_{\mathbf{P}} [\mathbf{J}_{t+1} \mathbf{J}_{t+1}^\top - \mathbf{J}_t \mathbf{J}_t^\top | \mathbf{z}_t, \mathbf{J}_t] &= -\beta \tilde{\eta} [\mathbf{Q}(\mathbf{J}_t^\top \mathbf{z}_t, \mathbf{J}_t^\top \cdot) + \mathbf{Q}(\mathbf{J}_t^\top \mathbf{z}_t, \mathbf{J}_t^\top \cdot)^\top] + \beta^2 \tilde{\eta}^2 \mathbf{Q}(\mathbf{J}_t^\top \mathbf{z}_t, \cdot) \mathbf{Q}(\mathbf{J}_t^\top \mathbf{z}_t, \cdot)^\top \\ &\quad + \beta(1 - \beta) \tilde{\eta}^2 \mathbb{E}_{\mathbf{Q}} \left[ \sum_{\mu} z_{t,\mu}^2 [\mathbf{Q}(\mathbf{J}_t^\top \mathbf{e}_\mu, \cdot) \mathbf{Q}(\mathbf{J}_t^\top \mathbf{e}_\mu, \cdot)^\top] \right] \end{aligned} \quad (88)$$

where the  $\mathbf{e}_\mu$  are the coordinate basis vectors.

Recall that we define  $\mathbf{Q}$  via the equation

$$\mathbf{Q} = \sum_{\gamma} \mathbf{w}_\gamma \otimes \mathbf{M}_\gamma \quad (89)$$

where the  $\mathbf{M}_\gamma$  are i.i.d. symmetric matrices with variances  $V(\sigma_\gamma)$ . Therefore, averaging over  $\mathbf{Q}$ , the first two terms vanish and we have:

$$\begin{aligned} \mathbf{w}_\alpha^\top \mathbb{E}_{\mathbf{P}, \mathbf{Q}} [\mathbf{J}_{t+1} \mathbf{J}_{t+1}^\top - \mathbf{J}_t \mathbf{J}_t^\top | \mathbf{z}_t, \mathbf{J}_t] \mathbf{w}_\alpha &= \beta^2 \tilde{\eta}^2 \mathbb{E}_{\mathbf{M}_\alpha} [\mathbf{z}_t^\top \mathbf{J}_t^\top \mathbf{M}_\alpha^\top \mathbf{M}_\alpha \mathbf{J}_t \mathbf{z}_t] \\ &\quad + \beta(1 - \beta) \tilde{\eta}^2 \mathbb{E}_{\mathbf{M}_\alpha} \left[ \sum_{\mu} z_{t,\mu}^2 \mathbf{e}_\mu^\top \mathbf{J}_t^\top \mathbf{M}_\alpha^\top \mathbf{M}_\alpha \mathbf{J}_t \mathbf{e}_\mu \right] + O(D^{-1}) \end{aligned} \quad (90)$$

Conducting the average over  $\mathbf{z}_t$  gives us, as desired:

$$\mathbb{E}_{\mathbf{P}, \mathbf{Q}, \mathbf{z}} [\Delta_1 \hat{\lambda}_{\alpha,t}] = PD^2 V_z \text{tr} \left[ \frac{1}{D} \mathbf{J}_t^\top \mathbf{J}_t \right] \tilde{\eta}^2 \beta V(\sigma_\alpha) + O(D^{-1}) \quad (91)$$

### B.2 Second discrete derivative of J

Now we consider

$$\Delta_2 \hat{\sigma}_{\alpha,t} = \mathbf{w}_\alpha^\top [\mathbf{J}_{t+2} - 2\mathbf{J}_{t+1} + \mathbf{J}_t] \mathbf{v}_\alpha \quad (92)$$

We can re-write this as:

$$\begin{aligned} \mathbf{J}_{t+2} - 2\mathbf{J}_{t+1} + \mathbf{J}_t &= -\tilde{\eta} [\mathbf{Q}((\mathbf{J}_{t+1} - \mathbf{J}_t)^\top \mathbf{P}_{t+1} \mathbf{z}_t, \cdot) + \mathbf{Q}(\mathbf{J}_t^\top \mathbf{P}_{t+1} (\mathbf{z}_{t+1} - \mathbf{z}_t), \cdot) \\ &\quad + \mathbf{Q}((\mathbf{J}_{t+1} - \mathbf{J}_t)^\top \mathbf{P}_{t+1} (\mathbf{z}_{t+1} - \mathbf{z}_t), \cdot)] - \tilde{\eta} \mathbf{Q}(\mathbf{J}_t^\top (\mathbf{P}_{t+1} - \mathbf{P}_t) \mathbf{z}_t, \cdot) \end{aligned} \quad (93)$$

Consider  $\mathbb{E}_{\mathbf{P}}[\mathbf{J}_{t+2} - 2\mathbf{J}_{t+1} + \mathbf{J}_t]$ . Most of the terms contain only one copy of  $\mathbf{P}_t$  or  $\mathbf{P}_{t+1}$ , so averaging gives a quantity that is “deterministic” - identical for fixed values of the product  $\beta\tilde{\eta}$ . The one non-trivial average is, to lowest order in  $\tilde{\eta}$ :

$$\mathbb{E}_{\mathbf{P}}[\mathbf{Q}((\mathbf{J}_{t+1} - \mathbf{J}_t)^\top \mathbf{P}_{t+1}(\mathbf{z}_{t+1} - \mathbf{z}_t), \cdot)] = \tilde{\eta}^2 \mathbb{E}_{\mathbf{P}}[\mathbf{Q}(\mathbf{Q}(\mathbf{J}_t^\top \mathbf{P}_t \mathbf{z}_t, \cdot)^\top \mathbf{P}_{t+1} \mathbf{J}_t \mathbf{J}_t^\top \mathbf{P}_t \mathbf{z}_t, \cdot)] + O(\tilde{\eta}^3) \quad (94)$$

Evaluating the average we have:

$$\mathbb{E}_{\mathbf{P}}[\mathbf{Q}((\mathbf{J}_{t+1} - \mathbf{J}_t)^\top \mathbf{P}_{t+1}(\mathbf{z}_{t+1} - \mathbf{z}_t), \cdot)] = \beta^2 \tilde{\eta}^2 \mathbf{Q}(\mathbf{Q}(\mathbf{J}_t^\top \mathbf{z}_t, \cdot)^\top \mathbf{J}_t \mathbf{J}_t^\top \mathbf{z}_t, \cdot) + \beta^2 (1 - \beta) \tilde{\eta}^2 \mathbf{Q}(\mathbf{N}(\mathbf{z}_t, \mathbf{J}_t) \mathbf{z}_t, \cdot) + O(\tilde{\eta}^3) \quad (95)$$

Where the matrix valued function  $\mathbf{N}(\mathbf{z}, \mathbf{J})$  is given by:

$$\mathbf{N}(\mathbf{z}, \mathbf{J})_{i\gamma} = \sum_{\beta, j} \mathbf{Q}_{\beta ij} \mathbf{J}_{\gamma j} \mathbf{z}_\gamma (\mathbf{J} \mathbf{J}^\top)_{\beta\gamma} \quad (96)$$

We can write  $\mathbb{E}_{\mathbf{P}}[\Delta_2 \hat{\lambda}_{\alpha, t}]$  as

$$\mathbb{E}_{\mathbf{P}}[\Delta_2 \hat{\lambda}_{\alpha, t}] = d_2(\mathbf{z}_t, \mathbf{J}_t, \beta\tilde{\eta}) - \beta^2 \tilde{\eta}^3 \mathbf{w}_\alpha^\top \mathbf{Q}(\mathbf{N}(\mathbf{z}_t, \mathbf{J}_t) \mathbf{z}_t, \mathbf{v}_\alpha) + O(\tilde{\eta}^4) \quad (97)$$

where the deterministic part  $d_2$  is given by

$$d_2(\mathbf{z}, \mathbf{J}, \tilde{\eta}) = \tilde{\eta}^2 \mathbf{w}_\alpha^\top [\mathbf{Q}(\mathbf{z} \cdot \mathbf{Q}(\mathbf{J}^\top \mathbf{z}, \cdot), \mathbf{v}_\alpha) + \mathbf{Q}(\mathbf{J}^\top \mathbf{J} \mathbf{J}^\top \mathbf{z}, \mathbf{v}_\alpha) - \tilde{\eta} \mathbf{Q}(\mathbf{Q}(\mathbf{J}^\top \mathbf{z}, \cdot)^\top \mathbf{J} \mathbf{J}^\top \mathbf{z}, \mathbf{v}_\alpha)] + \tilde{\eta}^3 \mathbf{w}_\alpha^\top \mathbf{Q}(\mathbf{N}(\mathbf{z}_t, \mathbf{J}_t) \mathbf{z}_t, \mathbf{v}_\alpha) \quad (98)$$

The  $d_2$  term is the same for constant  $\beta\tilde{\eta}$ . In the batch-averaged setting, it has no dependence on batch size.

It remains to average the stochastic term over  $\mathbf{Q}$  and  $\mathbf{z}$ . Averaging over  $\mathbf{Q}$  first, we have

$$\mathbb{E}_{\mathbf{Q}}[\mathbf{w}_\alpha \cdot \mathbf{Q}(\mathbf{N}(\mathbf{z}, \mathbf{J}) \mathbf{z}, \mathbf{v}_\alpha)] = \mathbb{E}_{\mathbf{Q}}[[\mathbf{w}_\alpha \cdot \mathbf{Q}]_{ij} (\mathbf{v}_\alpha)_j \mathbf{Q}_{\beta ik} \mathbf{J}_{\gamma k} \mathbf{z}_\gamma (\mathbf{J} \mathbf{J}^\top)_{\beta\gamma} \mathbf{z}_\gamma] \quad (99)$$

Expanding  $\mathbf{J} \mathbf{J}^\top = \sum_{\beta} (\sigma_\beta)^2 \mathbf{w}_\beta \mathbf{w}_\beta^\top$ , we have

$$\mathbb{E}_{\mathbf{Q}}[\mathbf{w}_\alpha \cdot \mathbf{Q}(\mathbf{N}(\mathbf{z}, \mathbf{J}) \mathbf{z}, \mathbf{v}_\alpha)] = \sum_{\beta} \mathbb{E}_{\mathbf{Q}}[(\sigma_\beta)^2 [\mathbf{w}_\alpha \cdot \mathbf{Q}]_{ij} (\mathbf{v}_\alpha)_j [\mathbf{w}_\beta \cdot \mathbf{Q}]_{ik} \mathbf{J}_{\gamma k} \mathbf{z}_\gamma^2 (\mathbf{w}_\beta)_\gamma] \quad (100)$$

If  $\mathbf{z}$  is independent of  $\mathbf{J}$  we have

$$\mathbb{E}_{\mathbf{Q}, \mathbf{z}}[\mathbf{w}_\alpha \cdot \mathbf{Q}(\mathbf{N}(\mathbf{z}, \mathbf{J}) \mathbf{z}, \mathbf{v}_\alpha)] = \sigma_\alpha^3 V(\sigma_\alpha) P \mathbb{E}_{\mathbf{z}}[(\mathbf{w}_\alpha)^\top \text{diag}(\mathbf{z}^2) \mathbf{w}_\alpha] \quad (101)$$

This is a non-negative number. The magnitude depends on the correlation between  $\mathbf{w}_\sigma$  and  $\mathbf{z}$ , the singular values  $\sigma$ , and the magnitude of the projection of  $\mathbf{Q}$  in the appropriate eigenspace.

Finally, making the i.i.d. assumption on  $\mathbf{z}$  we have

$$\mathbb{E}_{\mathbf{Q}, \mathbf{z}}[\mathbf{w}_\alpha \cdot \mathbf{Q}(\mathbf{N}(\mathbf{z}, \mathbf{J}) \mathbf{z}, \mathbf{v}_\alpha)] = \hat{\sigma}_{\alpha, t}^3 V(\sigma_\alpha) P V_z + O(\tilde{\eta}^4) \quad (102)$$

In total, we have:

$$\mathbb{E}_{\mathbf{P}, \mathbf{Q}, \mathbf{z}}[\Delta_2 \hat{\sigma}_{\alpha, t}] = d_2(\beta\tilde{\eta}) - \beta^2 \tilde{\eta}^3 \hat{\sigma}_{\alpha, t}^3 V(\sigma_\alpha) P V_z + O(\tilde{\eta}^4) \quad (103)$$

where  $d_2(\tilde{\eta}) = \mathbb{E}_{\mathbf{z}, \mathbf{Q}}[d_2(\mathbf{z}, \mathbf{J}, \tilde{\eta})]$  from Equation 98. This concludes the proof of the theorem.

### B.3 Numerical results

In order to support the theory, we simulated a quadratic regression model with  $D = 400$ ,  $P = 600$ , with various  $\mathbf{Q}$  spectra  $V(\sigma)$ , and plotted the dynamics of  $\Delta_1 \hat{\lambda}$  and  $\Delta_2 \hat{\sigma}$  for the largest eigenvalues (Figure 11, averaged over 30 seeds). We compare the “flat” spectrum  $V(\sigma) = 1$  with the “shaped” spectrum  $V(\sigma) \propto \sigma$ . As predicted by the theory, the first derivative increases with  $B^{-1}$  for fixed  $\eta$ , while second derivative decreases. Theoretical fit is better for flat  $\mathbf{Q}$ . Both the increase and the decrease are more extreme for the shaped  $\mathbf{Q}$ .



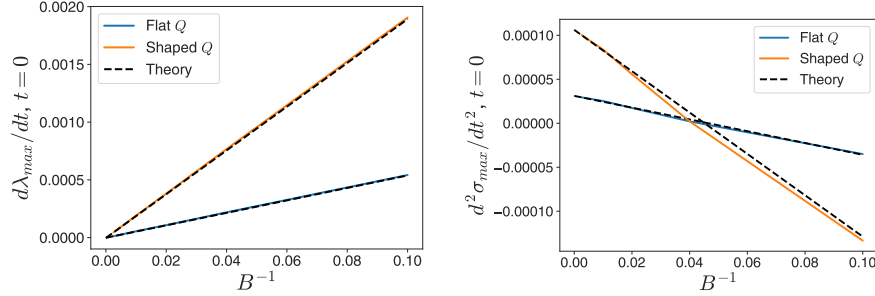


Figure 11: Eigenvalue discrete derivatives  $\Delta_1 \hat{\lambda}$  (left) and  $\Delta_2 \hat{\sigma}$  (right) for quadratic regression model,  $D = 400$ ,  $P = 600$ , averaged over 30 seeds. The Jacobian  $\mathbf{J}$  is initialized with random elements, and  $\mathbf{Q}$  has either a “flat” spectrum of  $V(\sigma) = 1$  (blue) or a “shaped” spectrum of  $V(\sigma) = \sigma$  (orange). First derivative increases as batch size  $B$  decreases, while second derivative decreases. Shaped  $\mathbf{Q}$  show stronger trends for both.

## C MNIST experiments

### C.1 Experimental setup

The experiments in Section 5.1 were all conducted using the first 2500 examples from MNIST. The labels were converted to 1 (odd digits) or  $-1$  (even digits), and the models were trained with MSE loss. The networks architecture was two fully connected hidden layers of width 256, with erf activation function. Inputs were pre-processed with ZCA.

For small batch sizes, networks were trained with a constant number of epochs. We trained for  $1.2 \cdot 10^6$  total samples (480 epochs) up to and including batch size 32. This was motivated by the observation that for small  $\eta$  and small  $B$ , dynamics was roughly universal for a fixed number of epochs for constant  $\eta/B$  (as is the case in the convex setting of (Paquette et al., 2021)). However, for larger batch sizes the dynamics is most similar for similar values of  $\eta$ , keeping the number of *steps* fixed. For batch size 32 and larger, models were trained for  $3.75 \cdot 10^4$  steps.

We also changed the learning rate sweep range in a batch-size dependent way. For small batch size  $B \leq 32$  we swept over a constant range in  $\eta/B$ , since this was the parameter which predicts divergence in the small batch setting. For larger batch sizes  $B \geq 32$  we swept over a constant range in  $\eta$  - chosen once again using the same  $\eta$  range as for  $B = 32$ . This let us efficiently explore both the small batch and large batch regimes in fine detail over  $\eta$  and  $B$ .

### C.2 Approximate vs exact $\mathcal{K}$

This setup was chosen to allow for exact computation of  $\mathcal{K}$  as per Equation ???. We computed the empirical NTK exactly, took its eigendecomposition, and used that to construct the matrix  $\mathbf{M} = (\mathbf{I} - \mathbf{A})^{-1/2} \mathbf{B} (\mathbf{I} - \mathbf{A})^{-1/2}$ . This is similar to  $(\mathbf{I} - \mathbf{A})^{-1} \mathbf{B}$  but is symmetric. We then computed the maximum eigenvalue of  $\mathbf{M}$  to obtain the instantaneous value of  $\mathcal{K}$ .

As in the convex case, the trace estimator of  $\mathcal{K}$  systematically underestimates the true value of  $\mathcal{K}$ , especially near  $\mathcal{K} = 1$  (Figure 12). Both quantities are still  $O(1)$  over a similar regime but quantitative prediction of largest stable learning rate is easier with exact value.

## D CIFAR experiments

### D.1 Experimental setup

The experiments in Section 5.2 were conducted on CIFAR10 using ResNet18 (He et al., 2016), with layer normalization and GeLU activation function. The models were trained with MSE loss and  $L^2$  regularization with  $\lambda = 5 \cdot 10^{-4}$  using momentum with parameter 0.9 and a cosine learning rate schedule. We trained with batch sizes  $2^k$  for  $k \in \{3, 4, \dots, 8\}$  on GPU. All models were trained for 200 epochs.

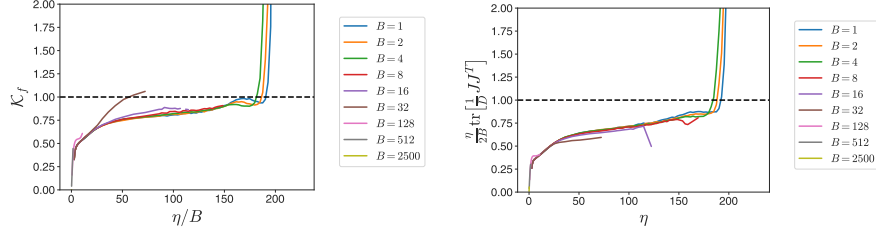


Figure 12: Exact computation of  $\mathcal{K}$  (left) vs. trace estimator (right) for FCN trained on MNIST. Trace estimate underestimates the true  $\mathcal{K}$ , especially as  $\mathcal{K}$  goes to a value near 1.

For each batch size  $B$ , we swept over constant normalized base learning rate  $\eta/B$  in the range  $[10^{-4}, 0.0125]$ , interpolating evenly in log space by powers of 2. For batch size 128, this corresponds to a range  $[0.0125, 1.6]$  in base learning rate  $\eta$ .

The measurements of largest eigenvalues were made with a Lanczos method as in (Ghorbani et al., 2019), from which we also obtained estimates of the trace of the full Hessian. The NTK trace was computed exactly using autodifferentiation.

## D.2 Phase plane plots

We can use the sweep over  $B$  and  $\eta/B$  to construct phase plane plots for the CIFAR experiments similar to those for MNIST in Section 5.1. Once again we see that the median estimated noise kernel norm (Figure 13, left) and the final error (Figure 13, right) are similar for constant  $\eta/B$  across batch sizes. We also see evidence that the universality is broken for both large  $\eta/B$  as well as large batch size  $B$ .

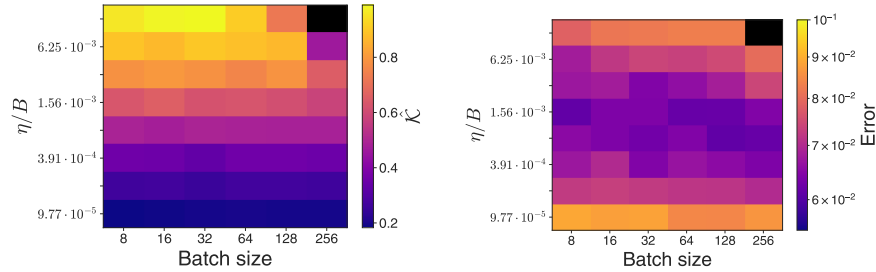


Figure 13: Phase planes for median  $\mathcal{K}$  (left) and final test error (right) for ResNet18 trained on CIFAR10.  $\mathcal{K}$  increases with increasing  $\eta/B$ . Statistics are consistent for a range of batch sizes for fixed  $\eta/B$ . Consistency breaks down at large  $\eta/B$  corresponding to values of  $\mathcal{K}$  close to 1, as well as for larger batch size.

## D.3 Largest eigenvalue dynamics

The learning rate and batch size ranges were chosen, in part, because they lead to dynamics which is well below the (deterministic) edge of stability. The dynamics of the largest eigenvalue  $\lambda_{max}$  of the full-dataset Hessian can be seen in Figure 14. The raw eigenvalue has an initial increase, a later decrease, a plateau, and finally a decrease (left). However, the normalized eigenvalue  $\eta_t \lambda_{max}$  increases and then decreases, and stays well below the edge of stability value of 2 (right). This suggests that the results of Section 5.2 can't be explained by the deterministic edge of stability. Note that the normalized values are computed using the instantaneous step size.

## D.4 Hessian trace ignoring $L^2$

In Figure 7, we showed that the full Hessian trace is a poor estimator for  $\mathcal{K}$ , and its dynamics is dominated by the  $L^2$  regularizer coefficient. Here we confirm that even removing the  $L^2$  regularizer during the computation of the Hessian trace does not fix the issue (Figure 15). Indeed the Hessian

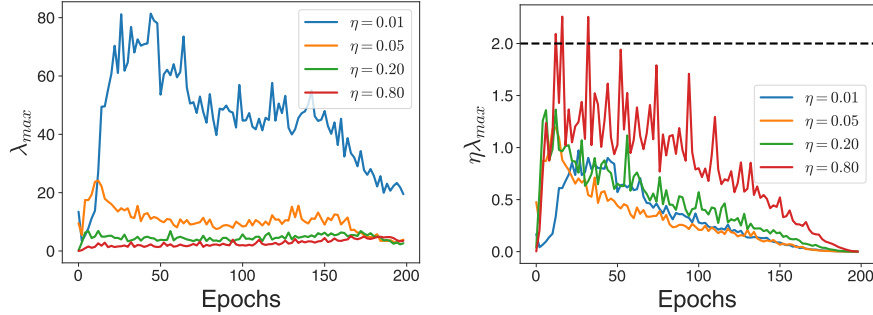


Figure 14: Maximum eigenvalue for ResNet18 on CIFAR. Raw eigenvalue increases at early times, then decreases to a steady value at intermediate times, and finally decreases at late times (left). Normalized eigenvalue is below the edge of stability ( $\eta_t \lambda_{max} < 2$ ) for all but the largest learning rate (right).

trace varies wildly over the course of learning, due to the contributions from the non-Gauss Newton part (Dauphin et al., 2024).

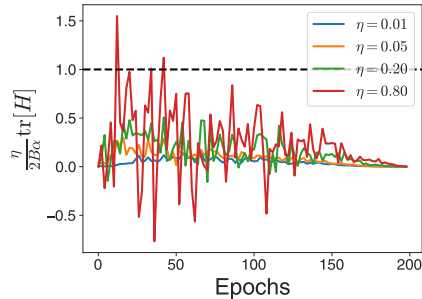


Figure 15: Hessian trace for CIFAR model, ignoring  $L^2$  regularization parameter. Even without including the parameter in the calculation, full Hessian trace is not a good approximator of  $\mathcal{K}$  and does not spend most of its time near 1.

## D.5 MLP-Mixer on CIFAR10

To provide additional evidence for the importance of the S-EOS, we also trained the MLP-Mixer model from (Tolstikhin et al., 2021), size S/16, on CIFAR10 to parallel the experiments from Figure 7 in the main text on a third architecture. We trained using SGD with momentum, MSE loss, batch size 128, and a cosine learning rate schedule with 1 epoch of linear warmup. The base learning rate was varied by factors of 2 from 0.00625 to 1.6. We find similar trends to ResNet:

- $\mathcal{K}$  **stays in range**  $[0.3, 1.0]$  **over a wide range of learning rates.** We vary learning rates by a factor of 128 and the typical  $\mathcal{K}$  value only varies by a factor of 3 (Figure 16, top left). This suggests there is some effect stabilizing its growth.
- $\lambda_{max}$  **remains far from the edge of stability.** Even for the largest learning rates,  $\eta \lambda_{max} \approx 1$ , far from the critical value of 2 (Figure 16, top right).
- $\mathcal{K}$  **close to 1 impedes training.** Larger learning rates spend more time with  $\mathcal{K}$  close to 1, which leads to slower improvements in loss and error rate (Figure 16, bottom row).

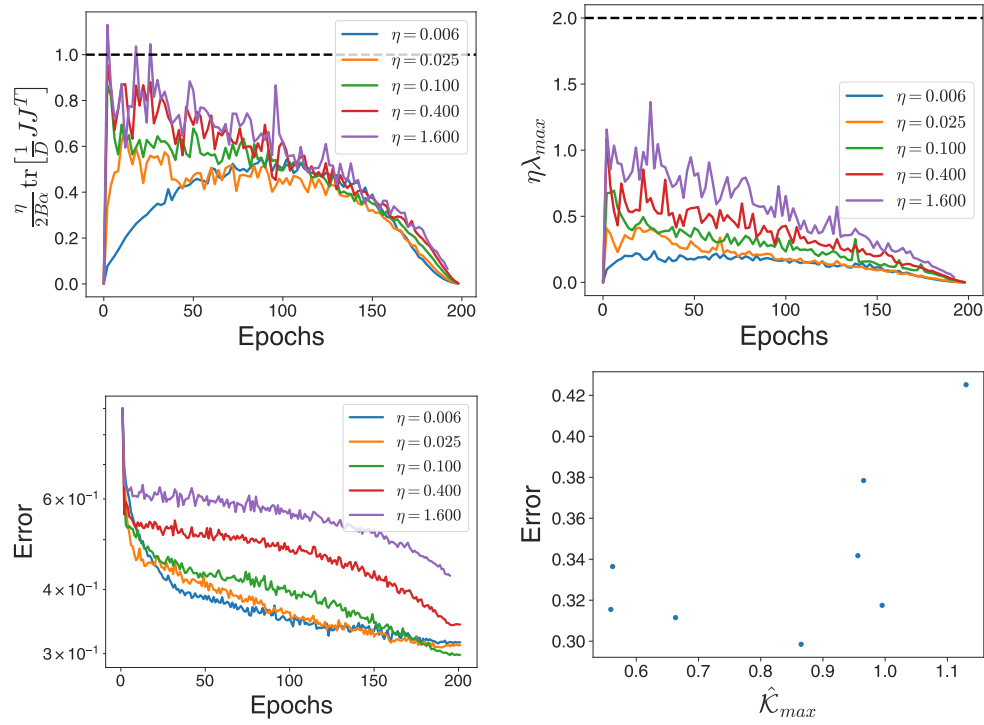


Figure 16: MLP-Mixer trained on CIFAR10. At large learning rates  $\hat{\mathcal{K}}$  is near 1 at early times, and at intermediate times values cluster over a large range of learning rates (top left). Maximum eigenvalue remains below edge of stability (top right). Learning is slow when  $\hat{\mathcal{K}}$  is near 1 (bottom left), and best performance is for intermediate values of  $\hat{\mathcal{K}}$  (bottom right).